Cognitive, synaptic and neuropathological changes in Alzheimer's brain-inoculated mice

Running Title: Impacts of Alzheimer-brain inoculation

Suzanne Lam[1,2], Susana Boluda[3,4], Anne-Sophie Hérard[1,2],
Fanny Petit[1,2], Sabiha Eddarkaoui[5], Karine Cambon[1,2],
The Brainbank Neuro-CEB Neuropathology Network[4,§], Jean-Luc Picq[1,2,6],
Luc Buée[5], Charles Duyckaerts[3,4], Stéphane Haïk[3,4], Marc Dhenain[1,2]

[1] Université Paris-Saclay, CEA, CNRS, Laboratoire des Maladies Neurodégénératives, 18 Route du Panorama, F-92265 Fontenay-aux-Roses, France.
[2] Commissariat à l'Energie Atomique et aux Energies Alternatives (CEA), Direction de la Recherche Fondamentale (DRF), Institut François Jacob, MIRCen, 18 Route du Panorama, F-92265 Fontenay-aux-Roses, France
[3] ICM Institut du Cerveau et de la Moelle épinière, CNRS UMR7225, INSERM U1127, Sorbonne Université, Hôpital de la Pitié-Salpêtrière, Paris, France
[4] Brainbank NeuroCEB Neuropathology Network: Plate-Forme de Ressources Biologiques, Bâtiment Roger Baillet, Hôpital de la Pitié-Salpêtrière, 47-83 boulevard de l'Hôpital, 75651 Paris Cedex 13.
[5] Université de Lille, Inserm, CHU-Lille, Lille Neuroscience & Cognition, Alzheimer & Tauopathies, LabEx DISTALZ, Rue Polonovski, 59045 Lille, France
[6] Laboratory of Cognitive Functioning and Dysfunctioning (DysCo), University of Paris 8, Saint-Denis 93526 cedex, France.

[§] Brainbank NeuroCEB Neuropathology Network: Franck Letournel (Angers), Marie-Laure Martin-Négrier (Bordeaux), Maxime Faisant (Caen), Catherine Godfraind (Clermont-Ferrand), Jean Boutonnat (Grenoble), Claude-Alain Maurage (Lille), Vincent Deramecourt (Lille), Mathilde Duchesne (Limoges), David Meyronet (Lyon), Tanguy Fenouil (Lyon), André Maués de Paula (Marseille), Valérie Rigau (Montpellier), Fanny Vandenbos-Burel (Nice), Danielle Seilhean (Paris) , Charles Duyckaerts (Paris), Susana Boluda (Paris), Isabelle Plu (Paris), Dan Christian Chiforeanu (Rennes), Annie Laquerrière (Rouen), Florent Marguet (Rouen), Béatrice Lannes (Strasbourg), Benoît Lhermitte (Strasbourg).

Corresponding author

Marc Dhenain, DVM, PhD
Commissariat à l'Energie Atomique et aux Energies Alternatives (CEA), Direction de la Recherche Fondamentale (DRF), Institut François Jacob, MIRCen, 18 Route du Panorama, F-92265 Fontenay-aux-Roses, France
E-mail: marc.dhenain@cea.fr

Abstract

Alzheimer's disease is characterized by lesions including extracellular amyloid-β plaques, intracellular tau accumulations, activated microglia around amyloid plaques and synaptic alterations that lead to cognitive impairments. Tau lesions occur in the form of tau-positive aggregates surrounding amyloid-β deposits leading to neuritic plaques, neuropil threads, and neurofibrillary tangles. The interactions between these lesions and their contribution to cognitive impairments are still debated.

In this study, through the intrahippocampal inoculation of human Alzheimer-brain extracts into an amyloid-β plaque-bearing mouse model, we induced amyloid plaques, Alzheimer-like tau-positive neuritic plaques, neuropil threads and neurofibrillary tangles that spread through the brain, microgliosis as well as synaptic and cognitive impairments in some animals.

Neuritic plaques, but not other tau-positive lesions, were detected in both non-inoculated and control-brain-inoculated amyloid-β plaque-bearing mice. Alzheimer-brain extracts inoculation further increased tau pathology within neuritic plaques. As opposed to the control-brain extract, Alzheimer-brain extracts induced neuropil threads and neurofibrillary tangles next to the inoculation site. These lesions also spread to connected brain regions such as the perirhinal/entorhinal cortex.

Different levels of synaptic loss and cognitive impairments were induced by inoculating two types of Alzheimer-brain extracts originating from slowly (clAD) or rapidly evolving forms of Alzheimer's disease (rpAD), although no difference in amyloid-β deposition, tau pathology and microgliosis was identified between clAD- and rpAD-inoculated animals.

A complementary analysis investigated relationships between synaptic or cognitive impairments and Alzheimer pathology. Synaptic defects were associated with the severity of tau lesions and with lower microglial load. Lower cognitive scores correlated with synaptic defects as well as with amyloid and tau pathologies in the hippocampus, and with tau lesions in the perirhinal/entorhinal cortex.

Taken together, this study shows that amyloid-β deposits are sufficient to induce tau pathology within neuritic plaques in Aβ plaque–bearing mice that do not overexpress tau. Alzheimer-brain extract inoculation however increases tau pathology within neuritic plaques, and induces neuropil threads and neurofibrillary tangles that spread in the brain. Inoculation of different human Alzheimer-brain extracts leads to different levels of synaptic loss and cognitive impairments. Synaptic loss and cognitive impairments are associated with multiple factors such as the severity of tau lesions and lower microglial activity, as well as amyloid deposition for cognitive changes. These results highlight that microglial activity may protect against synaptic loss.

Keywords

Alzheimer's disease; microglia; synaptotoxicity; tau; transmission

Introduction

Alzheimer's disease (AD) core lesions include amyloid-β (Aβ) plaques and intracellular tau accumulations that spread in a highly stereotyped pattern throughout the brain (Braak and Braak, 1991), neuroinflammation including microgliosis (Hansen *et al.*, 2018), and synaptic alterations (Terry *et al.*, 1991). The relationships between these lesions and how they lead to cognitive deficits are still partly unknown. In humans, cognitive impairments are strongly correlated with synaptic deficits (Terry *et al.*, 1991), with neocortical tau pathology but not as well with Aβ plaque load (Bennett *et al.*, 2004; Nelson *et al.*, 2012). Synaptic deficits have been associated with both tau (Hoover *et al.*, 2010; Pooler *et al.*, 2014; Spires-Jones and Hyman, 2014; Dejanovic *et al.*, 2018) and Aβ (Selkoe, 2002; Sivanesan *et al.*, 2013; Spires-Jones and Hyman, 2014) in mice and other experimental models. Microglia are key regulators of AD pathophysiology although their role is still debated. Several evidence (mostly in mouse models) suggest that increased activated microglia surrounding amyloid plaques are responsible for neuronal damage (Colonna and Butovsky, 2017). Also, microglia can engulf synapses in physiological conditions (Paolicelli *et al.*, 2011), as well as tau-positive synapses in pathological conditions (Dejanovic *et al.*, 2018). However, human genetic evidence, examplified by the lower incidence of AD in individuals with loss-of-function Trem2 mutations that impair microglial activation (Dourlen *et al.*, 2019), argues that microglia have a protective function.

Several studies have attempted to elucidate the interactions between all these elements of AD pathophysiology using transgenic mice overexpressing human Aβ or tau (with or without frontotemporal dementia mutations) (Gotz *et al.*, 2001; Pooler *et al.*, 2015; Bennett *et al.*, 2017). Over the last decade, new paradigms were established to induce widespread Aβ and tau pathologies in mice via the intracerebral injection of human AD brain extracts. These models provide a unique opportunity to assess relationships between AD core lesions and downstream neurodegenerative processes. In this study, we inoculated crude AD brain homogenates as well as control brain homogenates in the hippocampus of mice with high Aβ production. AD brain homogenates increased amyloid load at the inoculation site, increased tau lesions within neuritic plaques and induced neuropil threads and neurofibrillary tangles that spread in connected areas as the perirhinal/entorhinal cortex. Different levels of synaptic impairments and cognitive loss were induced by inoculating two different types of human AD brain extracts originating from slowly (clAD) or rapidly (rpAD) evolving forms of AD. No differences in amyloid, tau pathology or microgliosis were identified between the clAD- and rpAD-inoculated groups. In a complementary analysis, we investigated relationships between synaptic alterations or cognitive impairments and AD pathology using correlative studies. Synaptic defects were associated with the severity of tau lesions and to lower microglial load. Lower cognitive scores were associated with synaptic defects, amyloid deposits and tau pathology.

Material and methods

Human brain collection and characterization

Frozen brain samples (parietal cortex) from clinically different sporadic AD patients (four patients with classical slowly evolving forms of AD (clAD, disease duration of 5 to 8 years) and four with a rapidly evolving form of AD (rpAD, disease duration of 6 months to 3 years)) as well as age-matched control individuals (two cases) were collected from a brain donation program of the GIE NeuroCEB and the CNR-prion brain banks. Consent forms were signed by either the patients themselves or their next of kin in their name, in accordance with French bioethics laws. No case of hippocampal sclerosis was reported and all brain samples were PrPSc negative. Samples from clAD and rpAD brains were also negative for α-synuclein and TDP-43. All brain tissues were assessed by immunohistochemistry, as previously described in Gary et al. 2019 (Gary *et al.*, 2019) (Supplementary Methods 1).

Human brain homogenate preparation and characterization

Parietal cortex samples from each patient were individually homogenized at 10% weight/volume (w/v) in a sterile 1X Dulbecco's phosphate buffer solution in CK14 soft tissue homogenizing tubes at 5000 rpm for 20 sec (Precellys®, Bertin technologies). Individual brain homogenates were then sonicated on ice for 5 sec at 40% amplitude and centrifuged at 3000g for 5 min at +4°C. The resulting supernatant was aliquoted in sterile polypropylene tubes and stored at − 80 °C until use. Brain homogenates were then prepared by combining brain extracts from different patients. clAD and rpAD homogenates consisted in a combination of four brain extracts from the patients with clAD and rpAD, respectively. A third homogenate, considered as a control, was prepared from non-demented individuals (Ctrl, n=2 subjects).

Brain homogenates were characterized by biochemistry. Aβ levels were evaluated using the human V-PLEX kit Aβ Peptide Panel 1 (6E10) (MSD®) according to the manufacturer's recommendations (Supplementary Methods 2.1). Total tau and phosphot-tau181 were evaluated by ELISA according to the manufacturer's recommendations (Supplementary Methods 2.1). Tau was characterized by western blotting using AT100, 2H9, tau-Nter and tau-Cter antibodies (Supplementary Methods 2.2). Iba1 and GFAP proteins were also quantified by western blots (Supplementary Methods 2.2).

Transgenic mice

Mouse experiments were performed on the $APP_{swe}/PS1_{dE9}$ mouse model of amyloidosis (Garcia-Alloza *et al.*, 2006). Animals were studied eight or four months after intracerebral inoculation of the brain homogenates (at 8 and 4 months post-inoculation (mpi) respectively, n_{Ctrl}=15 and 11, n_{clAD}=15 and 14, n_{rpAD}=20 and 12). Wild-type littermates injected with the Ctrl brain sample were used as controls for the behavioral tests (at 8 and 4 mpi respectively, n_{WT}=12 and 6). All $APP_{swe}/PS1_{dE9}$ mice were born and bred in our center (Commissariat à l'Energie Atomique, centre de Fontenay-aux-Roses; European Institutions Agreement #B92-032-02). All animals were randomly assigned to the experimental groups. Males were exclusively used in this study. All experimental procedures were conducted in accordance with the European Community Council Directive 2010/63/UE and approved by local ethics committees (CEtEA-CEA DSV IdF N°44, France) and the French Ministry of Education and Research (A17_083 authorization).

Preparation of brain samples and stereotaxic surgery

10% Ctrl, clAD or rpAD individual brain homogenates were thawed on ice. Homogenates were then pooled together according to their group and the three resulting combined samples (Ctrl, clAD, rpAD) were sonicated (70% amplitude, 10 sec on/off; Branson SFX 150 cell disruptor sonicator, 3.17mm microtip probe Emerson, Bron) on ice in a sterile environment, extemporaneously before stereotaxic injection. Bilateral injections of brain samples were performed in the dorsal hippocampus of two-month old anesthethised mice (AP -2 mm, DV -2 mm, L +/- 1 mm from bregma, 2µl of sample administered at a 0.2µl/min rate) through a stereotaxic surgical procedure described in Supplementary Methods 3.

Behavioral evaluations

A battery of behavorial tests (elevated plus maze, a novel object recognition task in a V-maze, and a Morris water maze) was conducted at 8 mpi or 4 mpi on $APP_{swe}/PS1_{dE9}$ mice. Wild-type littermates injected with the Ctrl brain sample were used as controls for the tests. Mice were handled for 2 minutes per day, for 5 days prior to any test. Before each test, mice were habituated to the experimental room for 30 minutes. The experimenter was blind to mouse groups. Performances were recorded using a tracking software (EthoVision XT14, Noldus) (Supplementary Methods 4).

Animal sacrifice and brain preparation for histology

Mice were sacrificed at 8 or 4 mpi, after the behavioural tests, with an intraperitoneal injection of a lethal dose of pentobarbital (100 mg/kg; Exagon, Axience). They were perfused intracardiacally with cold sterile 0.1M PBS for 4 minutes, at a rate of 8 ml/min. The brain was extracted and post-fixed in 4% paraformaldehyde for 48 hours at +4°C, transferred in a 15% sucrose solution for 24 hours and in a 30% sucrose solution for 48 hours at +4°C for cryoprotection. Serial coronal sections of 40 µm were performed with a microtome (SM2400, Leica Microsystem) and stored at -20°C in a storing solution (glycerol 30%, ethylene glycol 30%, distilled water 30%, phosphate buffer 10%). Free-floating sections were rinced in a 0.1M PBS solution (10% Sigma-Aldrich® phosphate buffer, 0.9% Sigma-Aldrich® NaCl, distilled water) before use. Washing and incubation steps were performed on a shaker at room temperature unless indicated otherwise.

Immunohistochemistry for amyloid, tau, microgliosis and astrogliosis

Amyloid deposits were evaluated using a 4G8 labelling. Tau was evaluated using AT8 and AT100 labellings. Microgliosis was evaluated using Iba1 and CD68 antibodies. Astrocytes were stained with the GFAP antibody. Staining procedures are described in Supplementary Methods 5. Stained sections were scanned using an Axio Scan.Z1 and segmented using ImageJ-based automatic local thresholding methods to quantify 4G8, AT8, AT100, Iba1 and CD68 immunostainings (Supplementary Methods 5). In addition for the AT8 immunostaining, a quantification of neuritic plaques and AD-like neurofibrillary tangles was performed by manual counting (Supplementary Methods 5). A semi-quantitative analysis of neuropil threads was also performed by assigning a severity score based on the intensity and extent of AT8-positive staining in each ROI (Supplementary Methods 5).

Gallyas silver staining

Free-floating sections were mounted on Superfrost Plus (Thermo-Scientific®) slides and dried overnight prior to Gallyas staining according to a procedure described in Supplementary Methods 6.

Co-stainings of microglia and amyloid plaques

In order to evaluated microglial load surrounding amyloid plaques, microglia and amyloid plaque co-staining was performed according to a procedure described in Supplementary Methods 7. The method used to quantify microglial load around plaques is described in the same Supplementary Methods 7.

Evaluation of synaptic density

Synaptic density was evaluated in the hippocampus (CA1) and the perirhinal/entorhinal cortex of inoculated mice using a double immunolabelling of presynaptic (Bassoon) and postsynaptic (Homer1) markers. Free-floating sections were permeabilized in a 0.5% Triton X-100/0.1M PBS (Sigma-Aldrich®) solution for 15min. Slices were incubated with Bassoon (Abcam Ab82958, 1/200) and Homer1 (Synaptic systems 160003, 1/400) antibodies diluted in 3%BSA/PBST solution for 24 hours at +4°C. Incubation with secondary antibodies coupled to a fluorochrome (Alexa Fluor) diluted in a 3%BSA/0.1M PBS solution was then performed for 1h at room temperature. Sections were rinsed and mounted on Superfrost Plus (Thermo-Scientific®) slides with the Vectashield® mounting medium with a refractive index of 1.45. Images of stained sections were acquired using a Leica DMI6000 confocal optical microscope (TCS SPE) with a 63x oil-immersion objective (refractive index 1.518) and the Leica Las X software. A confocal zoom of 3 and a pinhole aperture fixed at 1 Airy were applied. Acquisition was performed in sequential mode with a sampling rate of 1024x1024 and a scanning speed of 700 Hz. Image resolution was 60 nm/pixel and the optical section was 0.896 µm. 26 separate planes with a 0.2 µm step were acquired. The excitation wavelengths were 594 nm or 633 nm. Image acquisition in the CA1 region was performed on 4 adjacent slices located between -1.82 mm and -3.28 mm from the bregma, with 2 images per slice. For the perirhinal/entorhinal cortex, 3 adjacent slices located between -3.28 mm and -4.24 mm from the bregma were analyzed, with 2 images acquired per slice. 3D deconvolution of the images was performed using the AutoQuant X3 software. The deconvoluted 8-bit images were analyzed using the ImageJ software, as described in Gilles et al (Gilles *et al.*, 2017). Briefly, automated 3D segmentation of the staining allowed to determine the volume occupied by Bassoon-positive or Homer-positive objects in the 3D space as well as the localization of the geometrical centroid or center of mass of the objects. Co-localization was determined by the detection of overlapping objects, and depended on the center-to-center distance and the percentage of co-localization volumes for each pair of objects.

Statistical analysis

Statistical analysis was performed using the GraphPad Prism software 8. Kruskal-Wallis test with Dunn's multiple comparisons were perfomed except when repeated measures were acquired in the behavioral tasks, in which case, a two-way repeated measures ANOVA with the Geisser-Greenhouse correction and Dunnett's multiple comparisons was carried out. Wilcoxon's signed-rank test was used to compare the time spent in the Morris Water maze quadrants with the theoretical value of 15 seconds (25% of trial duration). For comparisons between AD (clAD and rpAD mice as one AD group) and Ctrl mice, Mann-Whitney tests were conducted. For correlation studies, Spearman correlation test was performed. The significance level was set at $p<0.05$. Data are shown on scattered dot plots with mean ± standard error of the mean (s.e.m).

Data availability

The data that support the findings of this study are available from the corresponding author, upon reasonable request.

Results

Characterization of human brain homogenates

We prepared two brain homogenates from sporadic AD patients, with each homogenate consisting of a combination of four brain extracts from patients with either a rapidly evolving form of AD (rpAD) or patients with forms of AD that evolved more slowly (clAD). A third homogenate, considered as a control, was prepared from non-demented individuals (Ctrl, n=2 subjects). The characteristics of the selected subjects are presented in Supplementary Table 1 and Supplementary Fig. 1-2. The amounts of amyloid, tau and neuroinflammatory proteins slightly differed between the brain homogenates, as the rpAD homogenate displayed more total tau and phospho-tau181, but less $A\beta_{38}$ and $A\beta_{40}$ than the clAD one (Supplementary Fig. 2A-F). Iba1 and GFAP levels were similar in the two AD homogenates (Supplementary Fig. 2G-I).

Cognitive alterations in AD brain-inoculated mice

rpAD, clAD, and Ctrl brain homogenates were inoculated bilaterally (2 µl/site) in the dorsal hippocampus (CA1) of 2-month-old $APP_{swe}/PS1_{dE9}$ mice. This model expresses the endogenous murine tau protein isoforms and is not transgenic for any human tau. Inoculated mice were evaluated using a battery of behavioral tests at 8 mpi. An additional group of Ctrl-inoculated wild-type (WT) littermates was used as controls. First, we found that, compared to clAD and Ctrl brain inoculations, rpAD brain inoculation led to novel object recognition deficits as evaluated in an object-recognition task (V-maze test) (Fig. 1A-C). The test was divided into three phases (spread over 3 days). Following an habituation phase in an empty arena on day 1, two identical objects were added to the maze on day 2 (training phase). One of them was eventually removed and replaced by a novel object on day 3 (discrimination phase). Mice from each group showed similar exploratory activity, as suggested by comparable interest in the two identical objects during the training phase on day 2 (Fig. 1A), and similar distance travelled throughout the three days of test (Fig. 1B). During the novel object recognition evaluation on day 3, rpAD mice spent less time exploring the novel object, leading to a significantly lower discrimination index, compared to WT and $APP_{swe}/PS1_{dE9}$ clAD or Ctrl-inoculated mice (Fig. 1C, respectively, p=0.0018, 0.0082 and 0.0007). Spatial memory was then assessed using the Morris water maze test (Suppl Fig. 3A-C). During the training phase, no difference was observed between the groups suggesting that Ctrl, clAD and rpAD brain inoculations do not differentially impact spatial learning abilities in $APP_{swe}/PS1_{dE9}$ mice (Supplementary Fig. 3A-B). Spatial memory retention was then evaluated 72 hours after the last training test. All groups performed as well as the WT group by spending more time in the target quadrant than in the opposite one, suggesting that spatial memory is not impaired in $APP_{swe}/PS1_{dE9}$ Ctrl or AD-inoculated mice (Supplementary Fig. 3C). Moreover, the time spent both in the target quadrant and in the opposite one was significantly different from the theoretical value of 15 seconds, which corresponds to 25% of the trial duration, supporting the idea that all groups successfully memorized the platform location (Supplementary Fig. 3C). Anxiety levels were also evaluated using the general aversion of rodents to open spaces in the elevated plus maze test, which is a plus-shaped apparatus with two open and two enclosed arms. The different groups did not display differences in the distance travelled, the time spent leaning over the maze, as well as the time spent in open and enclosed arms or at their intersection in the center of the arena (Supplementary Fig. 3D-F). These results suggest that anxiety levels at 8 mpi are neither impacted by the $APP_{swe}/PS1_{dE9}$ genotype, nor by the intracerebral inoculation of AD brains. No difference in cognitive performance was observed at 4 mpi (Supplementary Fig. 4A-C, $n_{Ctrl}=11$, $n_{clAD}=14$, $n_{rpAD}=12$, $n_{WT}=6$).

Synaptotoxicity in AD brain-inoculated mice

Synaptic density was then evaluated in the hippocampus (CA1) and the perirhinal/entorhinal cortex of inoculated mice at 8 mpi, using a double immunolabelling of presynaptic (Bassoon) and postsynaptic (Homer) markers. The amount of colocalized punctas, an indicator of synaptic density, was decreased by 30% and 26% in rpAD mice compared to Ctrl and clAD mice, respectively, in the hippocampus (Fig. 1D, respectively p=0.0011 and 0.037). In the perirhinal/entorhinal cortex, lower synaptic density was observed in the rpAD group compared to the Ctrl group but not to the clAD group (Fig. 1E, respectively p=0.001 and 0.13). No difference in synaptic density was found between the Ctrl and clAD groups (Fig. 1D-E). Correlative studies showed that the discrimination index in the V-maze was correlated with synaptic defects in the CA1 (Fig. 1F, $r_{spearman\text{-}hip}=0.35$, p=0.02) but not in the perirhinal/entorhinal cortex (Fig. 1G, $r_{spearman\text{-}P/EC}=0.27$, p=0.29).

Acceleration of Aβ plaque deposition and induction of tau pathologies close to the injection site in AD brain-inoculated mice

At 8 mpi, AD brain inoculation led to an increase in amyloid plaque deposition in the hippocampus and in the region surrounding the alveus compared to Ctrl brain (Fig. 2, respectively for clAD and rpAD brains, p=0.0005 and p<0.0001 in the hippocampus, p<0.0001 and p<0.0001 in the alveus). The same changes were found at 4 mpi (Supplementary Fig. 4F-G). This suggests that the amyloid increase detected at 8 mpi (Fig. 2) already started at 4 mpi.

Three types of tau lesions occur in AD patients: tau-positive aggregates surrounding Aβ deposits leading to neuritic plaques, neuropil threads and neurofibrillary tangles. AD-like neuritic plaques (NPs) (Fig. 3A, G-J), neuropil threads (NTs) (Fig. 3B), neurofibrillary tangles (NFTs) (Fig. 3C-F) were all recapitulated in AD brain-inoculated $APP_{swe}/PS1_{dE9}$ mice.

At 8 mpi, neuritic plaques were detected in the hippocampus of AD- and Ctrl-inoculated mice (Fig. 3G-I, K-L). To further evaluate if human brain inoculation was necessary to induce these lesions, we performed an AT8 staining on old non-inoculated $APP_{swe}/PS1_{dE9}$ mice and also observed neuritic plaques (Fig. 3J). Quantification showed that neuritic plaque count was similar in AD- and Ctrl-inoculated mice (Fig. 3K). However, the AT8-positive area stained within neuritic plaques was larger in the two AD-inoculated groups compared to Ctrl animals (Fig. 3G-I and 3L, p=0.001 and p<0.0001, respectively for clAD and rpAD mice).

At 8 mpi, compared to the Ctrl-inoculated mice, AD-inoculated mice displayed an overall increase in tau lesions in the hippocampus (Fig. 3M-O, 3S; p=0.001 and p<0.0001 respectively for clAD and rpAD mice) and in the alveus (Fig. 3P-R, 3T; p=0.0035 and p<0.0001 respectively for clAD and rpAD mice), as revealed by an AT8-positive immunostaining directed against hyperphosphorylated tau. The same trends, although to a lesser extent, were reported at 4 mpi (Supplementary Fig. 4I-J). In AD-inoculated mice, AT8-positive neuropil threads were induced both in the hippocampus (Fig. 3U, p=0.0005 and p<0.0001 in clAD and rpAD mice, respectively) and the alveus (Fig. 3V, p=0.0036 and p<0.0001 in clAD and rpAD mice, respectively) whereas Ctrl-inoculated animals did not present these lesions. Moreover, AT8-positive NFTs were increased in the hippocampus of AD-inoculated mice as opposed to Ctrl-inoculated animals at 8 mpi (Fig. 3W, p=0.001 and p<0.0001 in clAD and rpAD mice, respectively).

Further evaluation of tau lesions revealed AT100 positive labelling in the forms of neuropil threads (Supplementary Fig. 5A, arrowheads) and NFTs (Supplementary Fig. 5A, arrow) in AD-inoculated mice. Quantification of the AT100 staining showed increased labelling in the alveus of AD-inoculated mice but not in the hippocampus (Supplementary Fig. 5B-C, p=0.0007 and 0.092 respectively). Gallyas silver staining revealed neuropil thread labelling

(Supplementary Fig. 5D) as well as amyloid plaques (Supplementary Fig. 5E). No quantification was performed as this technique reveals both tau and amyloid lesions.

Tau spreading in AD-brain inoculated mice

We then evaluated Aβ and tau lesions in the perirhinal/entorhinal brain regions that are connected to the hippocampus (Fig. 4A-B). Amyloid load was similar in the perirhinal/entorhinal cortex of rpAD, clAD and Ctrl mice (Fig. 4C-E, 4I, $p>0.05$). Aβ detected in the perirhinal/entorhinal cortex may thus only reflect the endogenous expression of the peptide in the $APP_{swe}/PS1_{dE9}$ model. Conversely, overall hyperphosphorylated tau lesions (AT8-positive area) were clearly increased in the perirhinal/entorhinal cortex of AD brain inoculated animals compared to Ctrl-inoculated ones (Fig. 4F-H, 4J, $p=0.0007$ and $p=0.0002$, respectively for clAD and rpAD mice). Neuritic plaque accumulation was increased in the perirhinal/entorhinal cortex of rpAD-inoculated mice compared to Ctrl mice (Fig. 6K, $p=0.038$). The AT8-positive area stained within neuritic plaques was larger in the perirhinal/entorhinal cortex of the two AD-inoculated groups compared to Ctrl animals suggesting that the neuritic plaques were more reactive in the AD groups (Fig. 6L, $p=0.0034$ and $p<0.0001$, respectively for clAD and rpAD mice). Neuropil threads and NFTs were detected in the perirhinal/entorhinal cortex of AD-inoculated mice but not in Ctrl-inoculated animals (Fig. 6M, neuropil thread accumulation for clAD and rpAD mice, $p=0.0003$ and $p=0.0002$; Fig. 6N, NTF accumulation for clAD and rpAD mice, $p=0.005$ and $p<0.0001$). These lesions were mainly found in the external layers II and III of the cortex (Fig 6F-H) that project to the dentate gyrus via the perforant pathway and to the CA1 region via the temporo-ammonic pathway, respectively. On the contrary, internal layers (*e.g.* layers V-VI) that receive projections from the CA1 region were not labelled. Other cortical regions such as the visual cortex also displayed neuropil threads, NFTs and neuritic plaques in clAD and rpAD mice (Supplementary Fig. 6A-B). As in the hippocampus, AT100 staining revealed tau lesions in the perirhinal/entorhinal cortex (Supplementary Fig. 7A-B) and a statistical difference in AT100-positive staining was detected between the ADs and Ctrl groups (Supplementary Fig. 7C, p=0.005). Gallyas staining was also positive for tau lesions (Supplementary Fig. 7D-E) and amyloid plaques (Supplementary Fig. 7D, 7F) in this region.

Studies at 4 mpi revealed an increased level of tau lesions in AD-inoculated mice next to the inoculation site (Supplementary Fig. 4I-J). However, no changes of tau lesions were detected in the perirhinal/entorhinal cortex at 4 mpi (Supplementary Fig. 4K). The increased presence of tau lesions at both sites at 8 mpi in AD-inoculated mice, while tau was not increased at 4 mpi in the perirhinal/entorhinal cortex, suggests that tau gradually spreads through the brain in a time-dependent manner. Consistently with the lack of amyloid spreading at 8 mpi (Fig. 4), no change in amyloid deposition was detected in the perirhinal/entorhinal cortex of Ctrl compared to AD-brain inoculated animals at 4 mpi (Supplementary Fig. 4H).

Neuroinflammatory response

Neuroinflammation was assessed by staining brain tissues using Iba1, a general marker for microglia as well as an anti-CD68 antibody that stains a lysosomal protein expressed at high levels by activated microglia and at low levels by resting microglia. Iba1 and CD68 stainings were positively correlated in the hippocampus and the perirhinal/entorhinal cortex (Supplementary Fig. 8A-B, $r_{\text{Spearman-hip}}=0.39$ and p=0.009, $r_{\text{Spearman-EC}}=0.53$ and p=0.0002). Quantification revealed similar levels of Iba1 (Fig. 5A-B) and CD68 (Fig. 5C-D) stained areas in the hippocampus or perirhinal/entorhinal cortex of clAD, rpAD and Ctrl groups ($p>0.05$; Kruskal-Wallis with Dunn’s multiple comparisons).

Visual observation of the stained sections suggested different levels of staining for Iba1 with some animals displaying high Iba1 labelling (Fig. 5G-H) and some others lower staining (Fig. 5K-L). Animals displaying high Iba1 labelling showed abundant activated microglia characterized by beading with spheroidal swellings of the processes and enlarged cell body with dystrophic ramifications (Fig. 5I, arrows) (Sanchez-Mejias *et al.*, 2016). These activated cells formed microglial clusters surrounding Aβ plaques (Fig. 5J). In contrast, mice with low Iba1 labelling (Fig. 5K-L) displayed highly ramified microglia, both close to and far from amyloid plaques (Fig. 5M and 5N respectively), which is consistent with a non-activated phenotype. As for Iba1, some animals displayed high CD68 labelling (Fig. 5O) and some others lower staining (Fig. 5P). Some clusters of CD68-stained microglia surrounded amyloid deposits (Fig. 5Q) while some others were not associated with amyloid deposits (Fig. 5R). Microglial activation was proposed to shield amyloid plaques off from neurons to prevent their toxicity (Condello *et al.*, 2015). Using confocal microscopy, we showed that, as expected, Iba1 stained microglia surrounding amyloid plaques (Supplementary Fig. 8C). We thus evaluated whether microglial load surrounding amyloid plaques differed following the inoculation of various brain extracts. We could not detect any differences in Iba1 staining around plaques in the different groups (Fig. 5E-F, $p>0.05$). This suggests no difference in the shielding effect in our three models of inoculation.

Finally, astrocyte reactivity (GFAP staining) was evaluated and no difference was detected between the groups in the hippocampus and in the perirhinal/entorhinal cortex (Supplementary Fig. 9).

Synaptic density is associated with Tau and reduced migroglial activation but not with Aβ pathology

No differences in amyloid (Fig. 2, 4), tau pathology (Fig. 3, 4) or microgliosis (Fig. 5) were identified between the rpAD- or clAD-inoculated group despite different levels of synaptic impairments (Fig. 1D-E). To further evaluate the origins of synaptic impairments, we took advantage of interindividual heterogeneity to assess the relationships between synaptic density and tau lesions, amyloid pathology and microgliosis. Synaptic density in the hippocampus (CA1) and in the perirhinal/entorhinal cortex was inversely correlated with global tau pathology in the same region (Fig. 6A, 6E, $r_{spearman\text{-}hip}$=-0.37, p=0.008 and $r_{spearman\text{-}P/EC}$=-0.32, p=0.03). Synaptic density in the perirhinal/entorhinal cortex was correlated with neuritic plaque count (Fig. 6F, $r_{spearman\text{-}P/EC}$=-0.50, p=0.0005), AT8-positive area stained within neuritic plaques (Fig. 6G, $r_{spearman\text{-}P/EC}$=-0.45, p=0.001), neuropil threads (Fig. 6H, $r_{spearman\text{-}P/EC}$=-0.43, p=0.003), and NFTs (Fig. 6I, $r_{spearman\text{-}P/EC}$=-0.38, p=0.011). This suggests that tau contributes to synaptic alterations. Synaptic density was not correlated with amyloid load in the hippocampus nor in the perirhinal/entorhinal cortex (Fig. 6B, 6J, p>0.05). A positive correlation was also reported between synapses and Iba1 staining in the hippocampus (Fig. 6C, $r_{spearman\text{-}hip}$=0.50, p=0.0002) and between synapses and Iba1 (Fig. 6K, $r_{spearman\text{-}P/EC}$=0.44, p=0.0018) or CD68 stainings (Fig. 6L, $r_{spearman\text{-}P/EC}$=0.57, p<0.0001) in the perirhinal/entorhinal cortex. No relationship between synapses and GFAP staining was observed in these regions (not shown).

Cognitive scores are associated with increased tau and amyloid loads

Cognitive changes were shown to be associated with synaptic impairments (Fig. 1F-G). We further investigated their relationships with AD pathology. Cognitive scores in the V-maze test were negatively correlated with tau pathology in both the hippocampus and the perirhinal/entorhinal cortex (global tau pathology (Fig. 7A-B, $r_{spearman\text{-}hip}$=-0.35, p=0.021 and $r_{spearman\text{-}P/EC}$=-0.42, p=0.0059), AT8-positive area stained within neuritic plaques (Fig. 7C-D, $r_{spearman\text{-}hip}$=-0.37, p=0.014 and $r_{spearman\text{-}P/EC}$=-0.42, p=0.006), neuropil threads (Fig. 7E-F, $r_{spearman\text{-}hip}$=-0.44, p=0.0039 and $r_{spearman\text{-}P/EC}$=-0.36, p=0.022), NFTs (Fig. 7G-H, $r_{spearman\text{-}hip}$=-0.34, p=0.032 and $r_{spearman\text{-}P/EC}$=-0.40, p=0.012)). Cognitive scores in the V-maze were also negatively correlated with amyloid load in the hippocampus, but not in the perirhinal/entorhinal cortex (Fig. 8A-B, $r_{spearman\text{-}hip}$=-0.48, p=0.001 and $r_{spearman\text{-}P/EC}$=-0.17, p=0.29). Finally, cognitive scores in the V-maze were positively correlated with microglial load stained by Iba1 in the hippocampus and perirhinal/entorhinal cortex (Fig. 8C-D, $r_{spearman\text{-}hip}$=0.34, p=0.028; $r_{spearman\text{-}P/EC}$=0.45, p=0.003) but not with CD68 staining (Fig. 8E-F, $r_{spearman\text{-}hip}$=0.07, p>0.6;

$r_{spearman\text{-}P/EC}$=0.16, p>0.3). No relationship between cognitive scores and astrocyte-associated GFAP staining was observed (not shown).

Discussion

Based on the intracerebral inoculation of crude AD brain homogenates into mice with high Aβ production, we produced a highly pathologically relevant AD model which develops amyloid plaques, tau lesions that spread in the brain, and in some cases synaptic and cognitive impairments.

A first part of our study was dedicated to compare the impact of the inoculation of Ctrl and two AD brain extracts (*e.g.* rapidly (rpAD) or slowly evolving forms (clAD) of AD). Comparison of Ctrl versus AD-inoculated mice (rpAD or clAD) showed that as expected (Di Fede *et al.*, 2018; Gary *et al.*, 2019), amyloid load was increased in the hippocampus following AD brain intrahippocampal inoculation.

Neuritic plaques were detected in AD-inoculated mice as well as in Ctrl-inoculated mice. We evaluated neuritic plaques in aged non-inoculated mice and found that they also displayed these lesions. This result is consistent with reports showing that neuritic plaques occur spontaneously with age in $APP_{swe}/PS1_{dE9}$ mice (Metaxas *et al.*, 2019). It suggests that β-amyloid plaques, *per se*, are sufficient to induce neuritic plaques. In humans, different forms of amyloid plaques, including non-Aβ ones, can also induce tau lesions in surrounding neurites (Duyckaerts *et al.*, 2018). Our study moved one step forward by showing that the density of tau lesions within neuritic plaques was higher in AD-inoculated mice compared with Ctrl-inoculated animals. Taken together, this highlights that amyloid plaques create a microenvironment that induces tau lesions within neuritic plaques, and that such lesions are amplified by the exposure to human AD brain, presumably because of exogenous pathological tau seeds.

Unlike neuritic plaques, neuropil threads and NFTs were not detected in Ctrl brain-inoculated mice. They were induced next to the inoculation site in the AD-inoculated animals. In addition, they spread from the inoculated site to connected brain regions such as the perirhinal/entorhinal cortex.

Following the comparison between Ctrl- and AD-inoculated mice, we compared mice inoculated with rpAD and clAD brain extracts. We provided the first experimental evidence that the intracerebral inoculation of these different AD brain extracts can induce different levels of synaptic loss and cognitive alterations. Group comparisons however did not show any differences between amyloid, tau or neuroinflammation levels between rpAD or clAD animals. Synaptic/cognitive differences may thus be related to a biological parameter that was not captured by our study, or also emerge from multiple causes.

In a second part of the study, we thus decided to assess relationships between synaptic or cognitive impairments and amyloid, tau, and microgliosis. At 8 mpi, synaptic deficits in the hippocampus (CA1) and the perirhinal/entorhinal cortex were significantly associated with global tau pathology. In the perirhinal/entorhinal cortex, *i.e.* at distance from the inoculation site, they were also correlated with AT8-positive area stained within neuritic plaques, neuropil threads and NFTs. These results, in a model that is not based on tau overexpression, strongly support that tau pathology contributes to synaptic alterations.

Synaptic loss was also associated with a reduction of microgliosis in the hippocampus (for Iba1 staining), but also at distance from the brain extract inoculation site in the perirhinal/entorhinal cortex (for both Iba1 and CD68 stainings). Controversial results are reported in the literature regarding the impact of microglial activation on AD-related neurodegenerative processes. In contradiction with our results, several studies showed that synaptic alterations are associated with increased microglial activation in amyloid-plaque bearing models (Spangenberg *et al.*, 2016) as well as in mice overexpressing human tau (Leyns *et al.*, 2017; Dejanovic *et al.*, 2018).

On the contrary, several evidence in mouse models with genetic-related microglial impairments (*e.g.* Trem2 deficient mice) (Leyns *et al.*, 2019; Lee *et al.*, 2021) or models with microglia depletion (Clayton *et al.*, 2021) suggest that microglial activation is protective. Our study supports a protective effect of microglial activation in, for the first time, a mouse model without genetic or chemical manipulation of microglia. In humans, genetic evidence examplified by the large effect of the loss-of-function Trem2 mutations on AD risk and on microglial function, argues that microglia have a protective function that lowers the incidence of AD (Hansen *et al.*, 2018). In non-genetic cases of AD, some studies (Streit *et al.*, 2009), but not all (Perez-Nievas *et al.*, 2013), also outlined the potential protective function of microglia.

One unexpected finding of our study is the weak association between synaptic changes and amyloid plaques. This does not rule out the well-described link between synaptic alterations and Aβ (Selkoe, 2002; Sivanesan *et al.*, 2013). In our experiments, we studied Aβ plaque-bearing mice and it is possible that Aβ-related impairments of synaptic function occurred in all experimental groups.

Relationships between cognitive impairments and Alzheimer pathology were also assessed in our study. Cognitive alterations at 8 mpi were correlated with synaptic defects in the hippocampus. They were also associated with the severity of amyloid and tau pathologies (overall tau pathology, neuritic plaque counts, AT8-positive area stained within neuritic plaques, neuropil threads, and NFTs) in the hippocampus, with these tau lesions in the perirhinal/entorhinal cortex as well as with lower Iba1-positive microglial load in the hippocampus and perirhinal/entorhinal cortex. This analysis underlines the potential role of amyloid and parameters linked to synaptic changes (tau/microgliosis) in cognitive impairments.

In our study, although synaptic and cognitive differences were found between rpAD and clAD animals, we did not detect rpAD/clAD group differences for amyloid, tau or microgliosis. One possible explanation supported by our results is that synaptic and cognitive impairments resulted from multifactorial and interacting causes and that small differences below the significance threshold for several factors (*e.g.* tau, microgliosis, amyloid) might entail dramatic changes in synapse integrity and cognition. Another possibility, that we cannot rule out, is that a biological parameter that was not detected by our experiments had a major contribution to the differences between rpAD and clAD animals. Neuroinflammatory factors such as C1q, C3 or IL-33 modulate synapse density by altering their formation and elimination (Dejanovic *et al.*, 2018; Litvinchuk *et al.*, 2018; Wilton *et al.*, 2019; Wang *et al.*, 2021). Although we did not attempt here to characterize the cytokinic profiles of our inocula, we cannot rule out that they contained distinct concentrations or panels of pro- and anti-inflammatory cytokines that may have influenced synapse integrity.

The intracerebral inoculation of human brain extracts in mice was shown to provide pathologically relevant AD models. Indeed, injection of either AD brain homogenates (Condello *et al.*, 2015) or highly aggregated human wild-type tau from sarkosyl-insoluble AD brain extracts (Audouard *et al.*, 2016; Guo *et al.*, 2016) can induce tau aggregates in wild-type mice. Moreover, mice with high Aβ production inoculated with sarkosyl-insoluble brain extracts from AD brains display both amyloid and tau pathologies. For the first time here, we used a strategy based on the inoculation of crude AD brain homogenates into mice with high Aβ production to induce tau lesions, amyloid plaques and downstream events including synaptic loss and cognitive impairments. Altogether, this model will be helpful to assess interactions between AD core lesions and neurodegenerative processes, as well as to evaluate new therapies targeting multiple AD hallmarks.

As a conclusion, we showed that tau-positive neuritic plaques, but not other tau lesions, can occur in old non-inoculated Aβ plaque–bearing mice or in mice inoculated with Ctrl brain extracts. We also showed that intracerebral injection of human AD brain extracts into an Aβ plaque–bearing mouse model that does not overexpress tau can recapitulate amyloid and tau lesions (Supplementary Table 2). AD brain extract inoculation increased tau pathology within neuritic plaques, and induced neuropil threads and NFTs that spread in the brain. Inoculation of different human AD brain extracts led to different levels of synaptic loss and cognitive impairments. Synaptic loss was associated with the severity of tau lesions which highlights the contribution of tau to synaptic pathology in a model that does not rely on the genetic manipulation of tau protein. Synaptic defects were also associated with lower microglial load in a model that does not rely on drastic genetic or chemical-based reduction of microglia. This indicates that microglial activity may protect against synaptic loss. Cognitive defects were associated with synaptic impairments, with tau lesions and also with amyloid deposition. Altogether these results highlight the multifactorial origin of cognitive impairments. Finally, the finding that microglial activity may protect against synaptic loss may have potential applications and supports further studies to assess the effect of anti-inflammatory therapies in subjects at risk for Alzheimer’s disease.

Acknowlegements

We thank Martine Guillermier and Mylène Gaudin for surgical expertise during inoculation of brain extracts to animals. We thank Nicolas Heck for his help in synapse quantification, and Nicolas Sergeant for a critical review of this article. We thank the donors and the Brain Donation Program of the "The Brainbank Neuro- CEB Neuropathology Network" run by a consortium of Patient Associations: ARSLA (association for research on amyotrophic lateral sclerosis), CSC (cerebellar ataxias), Fondation ARSEP (association for research on multiple sclerosis), France DFT (fronto-temporal dementia), Fondation Vaincre Alzheimer, France Parkinson, with the support of Fondation Plan Alzheimer and IHU A-ICM for providing the brain samples used in this study.

Funding

The project was funded by the Association France-Alzheimer. It was performed in a core facility supported by/member of NeurATRIS - ANR-11-INBS-0011. It was also supported by internal funds from the Laboratory of Neurodegenerative Diseases and MIRCen.

Author contributions

S.L., A.S.H., F.P., and M.D. contributed to the study conception and design. N.N.N., C.D. provided the human brain samples. N.N.N., S.L., S.B., C.D. and S.H. characterized the human brain samples. S.L., M.G. and M.G. performed the inoculations in mice. S.L. and K.C. designed and performed cognitive evaluations, A.S.H., F.P., and S.L. designed and performed the immunohistological analysis in animals. A.S.H., S.E., L.B., and S.L. performed biochemical analysis. S.L., A.S.H., and M.D. wrote the manuscript. All authors commented on previous versions of the manuscript. All authors read and approved the final manuscript.

Competing interests

The authors declare no competing interests.

References

Audouard E, Houben S, Masaracchia C, Yilmaz Z, Suain V, Authelet M, et al. High-molecular-weight paired helical filaments from Alzheimer brain induces seeding of wild-type mouse tau into an argyrophilic 4R Tau pathology in vivo. Am J Pathol 2016; 186(10): 2709-22.

Bennett DA, Schneider JA, Wilson RS, Bienias JL, Arnold SE. Neurofibrillary tangles mediate the association of amyloid load with clinical Alzheimer disease and level of cognitive function. Arch Neurol 2004; 61(3): 378-84.

Bennett RE, DeVos SL, Dujardin S, Corjuc B, Gor R, Gonzalez J, et al. Enhanced Tau aggregation in the presence of amyloid beta. Am J Pathol 2017; 187(7): 1601-12.

Braak H, Braak E. Neuropathological stageing of Alzheimer related changes. Acta Neuropathol 1991; 82: 239-59.

Clayton K, Delpech JC, Herron S, Iwahara N, Ericsson M, Saito T, et al. Plaque associated microglia hyper-secrete extracellular vesicles and accelerate tau propagation in a humanized APP mouse model. Mol Neurodegener 2021; 16(1).

Colonna M, Butovsky O. Microglia function in the central nervous system during health and neurodegeneration. Annu Rev Immunol 2017; 35: 441-68.

Condello C, Yuan P, Schain A, Grutzendler J. Microglia constitute a barrier that prevents neurotoxic protofibrillar Abeta42 hotspots around plaques. Nat Commun 2015; 6: 6176.

Dejanovic B, Huntley MA, De Maziere A, Meilandt WJ, Wu T, Srinivasan K, et al. Changes in the synaptic proteome in tauopathy and rescue of Tau-induced synapse loss by C1q antibodies. Neuron 2018; 100(6): 1322-+.

Di Fede G, Catania M, Maderna E, Ghidoni R, Benussi L, Tonoli E, et al. Molecular subtypes of Alzheimer's disease. Sci Rep 2018; 8: 3269.

Dourlen P, Kilinc D, Malmanche N, Chapuis J, Lambert JC. The new genetic landscape of Alzheimer's disease: from amyloid cascade to genetically driven synaptic failure hypothesis? Acta Neuropathol 2019; 138(2): 221-36.

Duyckaerts C, Sazdovitch V, Ando K, Seilhean D, Privat N, Yilmaz Z, et al. Neuropathology of iatrogenic Creutzfeldt-Jakob disease and immunoassay of French cadaver-sourced growth hormone batches suggest possible transmission of tauopathy and long incubation periods for the transmission of Abeta pathology. Acta Neuropathol 2018; 135(2): 201-12.

Garcia-Alloza M, Robbins EM, Zhang-Nunes SX, Purcell SM, Betensky RA, Raju S, et al. Characterization of amyloid deposition in the APPswe/PS1dE9 mouse model of Alzheimer disease. Neurobiol Dis 2006; 24(3): 516-24.

Gary C, Lam S, Herard AS, Koch JE, Petit F, Gipchtein P, et al. Encephalopathy induced by Alzheimer brain inoculation in a non-human primate. Acta Neuropathol Commun 2019; 7(126).

Gilles JF, Dos Santos M, Boudier T, Bolte S, Heck N. DiAna, an ImageJ tool for object-based 3D co-localization and distance analysis. Methods 2017; 115: 55-64.

Gotz J, Chen F, van Dorpe J, Nitsch RM. Formation of neurofibrillary tangles in P301l tau transgenic mice induced by Abeta 42 fibrils. Science 2001; 293(5534): 1491-5.

Guo JL, Narasimhan S, Changolkar L, He ZH, Stieber A, Zhang B, et al. Unique pathological tau conformers from Alzheimer's brains transmit tau pathology in nontransgenic mice. J Exp Med 2016; 213(12): 2635-54.

Hansen DV, Hanson JE, Sheng M. Microglia in Alzheimer's disease. J Cell Biol 2018; 217(2): 459-72.

Hoover BR, Reed MN, Su J, Penrod RD, Kotilinek LA, Grant MK, et al. Tau mislocalization to dendritic spines mediates synaptic dysfunction independently of neurodegeneration. Neuron 2010; 68(6): 1067-81.

Lee S-H, Meilandt WJ, Xie L, Gandham VD, Ngu H, Barck KH, et al. Trem2 restrains the enhancement of tau accumulation and neurodegeneration by b-amyloid pathology. Neuron 2021; 109: 1–19.

Leyns CEG, Gratuze M, Narasimhan S, Jain N, Koscal LJ, Jiang H, et al. TREM2 function impedes tau seeding in neuritic plaques. Nat Neurosci 2019; 22(8): 1217-22.

Leyns CEG, Ulrich JD, Finn MB, Stewart FR, Koscal LJ, Serrano JR, et al. TREM2 deficiency attenuates neuroinflammation and protects against neurodegeneration in a mouse model of tauopathy. Proc Natl Acad Sci USA 2017; 114(43): 11524-9.

Litvinchuk A, Wan YW, Swartzlander DB, Chen FD, Cole A, Propson NE, et al. Complement C3aR Inactivation Attenuates Tau Pathology and Reverses an Immune Network Deregulated in Tauopathy Models and Alzheimer's Disease. Neuron 2018; 100(6): 1337-+.

Metaxas A, Thygesen C, Kempf SJ, Anzalone M, Vaitheeswaran R, Petersen S, et al. Ageing and amyloidosis underlie the molecular and pathological alterations of tau in a mouse model of familial Alzheimer's disease. Sci Rep 2019; 9: 15758.

Nelson PT, Alafuzoff I, Bigio EH, Bouras C, Braak H, Cairns NJ, et al. Correlation of Alzheimer disease neuropathologic changes with cognitive status: a review of the literature. J Neuropath Exp Neur 2012; 71(5): 362-81.

Paolicelli RC, Bolasco G, Pagani F, Maggi L, Scianni M, Panzanelli P, et al. Synaptic Pruning by Microglia Is Necessary for Normal Brain Development. Science 2011; 333(6048): 1456-8.

Perez-Nievas BG, Stein TD, Tai HC, Dols-Icardo O, Scotton TC, Barroeta-Espar I, et al. Dissecting phenotypic traits linked to human resilience to Alzheimer's pathology. Brain 2013; 136: 2510-26.

Pooler AM, Noble W, Hanger DP. A role for tau at the synapse in Alzheimer's disease pathogenesis. Neuropharmacology 2014; 76: 1-8.

Pooler AM, Polydoro M, Maury EA, Nicholls SB, Reddy SM, Wegmann S, et al. Amyloid accelerates tau propagation and toxicity in a model of early Alzheimer's disease. Acta Neuropathol Commun 2015; 3: Article number 14.

Sanchez-Mejias E, Navarro V, Jimenez S, Sanchez-Mico M, Sanchez-Varo R, Nunez-Diaz C, et al. Soluble phospho-tau from Alzheimer's disease hippocampus drives microglial degeneration. Acta Neuropathol 2016; 132(6): 897-916.

Selkoe DJ. Alzheimer's disease is a synaptic failure. Science 2002; 298(5594): 789-91.

Sivanesan S, Tan A, Rajadas J. Pathogenesis of abeta oligomers in synaptic failure. Curr Alzh Res 2013; 10(3): 316e23.

Spangenberg EE, Lee RJ, Najafi AR, Rice RA, Elmore MRP, Blurton-Jones M, et al. Eliminating microglia in Alzheimer's mice prevents neuronal loss without modulating amyloid-beta pathology. Brain 2016; 139: 1265-81.

Spires-Jones TL, Hyman BT. The intersection of amyloid beta and tau at synapses in Alzheimer's disease. Neuron 2014; 82(4): 756-71.

Streit WJ, Braak H, Xue QS, Bechmann I. Dystrophic (senescent) rather than activated microglial cells are associated with tau pathology and likely precede neurodegeneration in Alzheimer's disease. Acta Neuropathol 2009; 118(4): 475-85.

Terry RD, Masliah E, Salmon DP, Butters N, DeTeresa R, Hill R, et al. Physical basis of cognitive alterations in Alzheimer's disease: synapse loss is the major correlate of cognitive impairment. Ann Neurol 1991; 30(4): 572-80.

Wang Y, Fu WY, Cheung K, Hung KW, Chen CP, Geng HY, et al. Astrocyte-secreted IL-33 mediates homeostatic synaptic plasticity in the adult hippocampus. Proc Natl Acad Sci USA 2021; 118(1).

Wilton DK, Dissing-Olesen L, Stevens B. Neuron-Glia signaling in synapse elimination. Annu Rev Neurosci 2019; 42: 107-27.

FIGURES

Figure 1

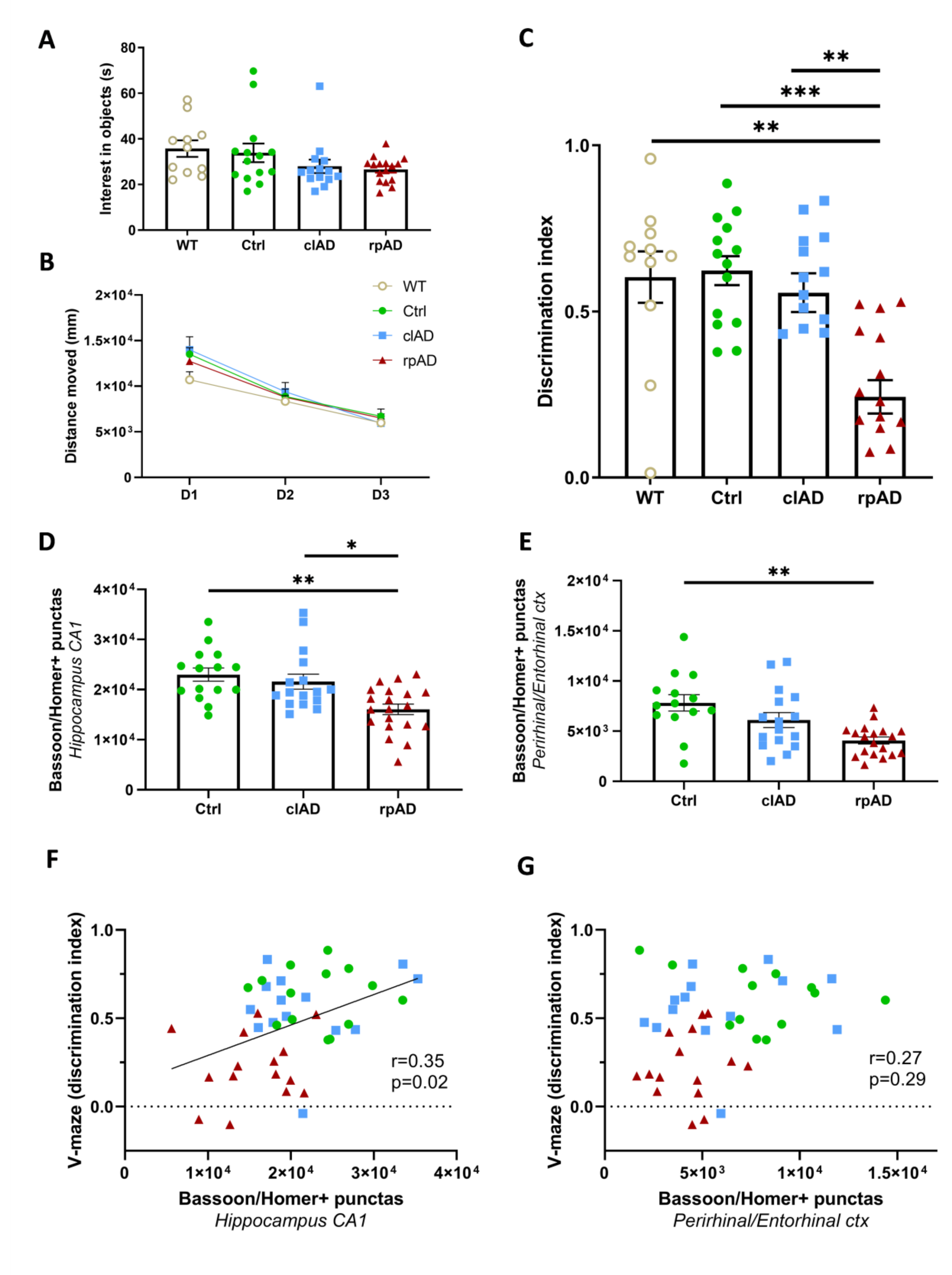

Figure 1. Object recognition deficits and synaptotoxicity in the rpAD-inoculated mice. Object recognition performances were evaluated at 8 mpi in a V-maze. WT mice and

$APP_{swe}/PS1_{dE9}$ mice inoculated with Ctrl, clAD or rpAD brain extracts had comparable exploratory activity, as suggested by the time spent on exploring the objects (A, $p>0.05$; Kruskal-Wallis with Dunn's multiple comparisons) and the distance moved throughout the 3-day test (B, for the days: $F_{(1.75,\ 89.47)} = 91.97$, $p<0.0001$; for the groups: $F_{(3,\ 51)} = 0.89$, $p=0.45$; two-way repeated measures ANOVA with the Geisser-Greenhouse correction and Dunnett's multiple comparisons). During the novel object recognition evaluation, rpAD-inoculated mice spent less time exploring the novel object, as suggested by a lower discrimination index, compared to WT and $APP_{swe}/PS1_{dE9}$ clAD or Ctrl-inoculated mice (C, respectively, $p=0.0018$, 0.0082 and 0.0007; Kruskal-Wallis with Dunn's multiple comparisons). (D-E) Quantification of Bassoon and Homer colocalization revealed a decrease in synaptic density in rpAD mice in the CA1 (D, respectively $p=0.0011$ and 0.037; Kruskal-Wallis with Dunn's multiple comparisons) and perirhinal/entorhinal cortex (E, respectively $p=0.001$ and 0.13; Kruskal-Wallis with Dunn's multiple comparisons), compared to Ctrl and/or clAD-inoculated mice at 8 mpi. V-maze cognitive scores (discrimination index) were correlated with synaptic defects in the CA1 (F, $r_{spearman\text{-}hip}=0.35$, $p=0.02$) but not in the perirhinal/entorhinal cortex (G, $r_{spearman\text{-}P/EC}=0.27$, $p=0.29$). $n_{Ctrl}=15$, $n_{clAD}=15$, $n_{rpAD}=20$, $n_{WT}=12$ mice. *$p<0.05$; **$p<0.01$ ***$p<0.001$; Data are shown as mean ± s.e.m.

Figure 2

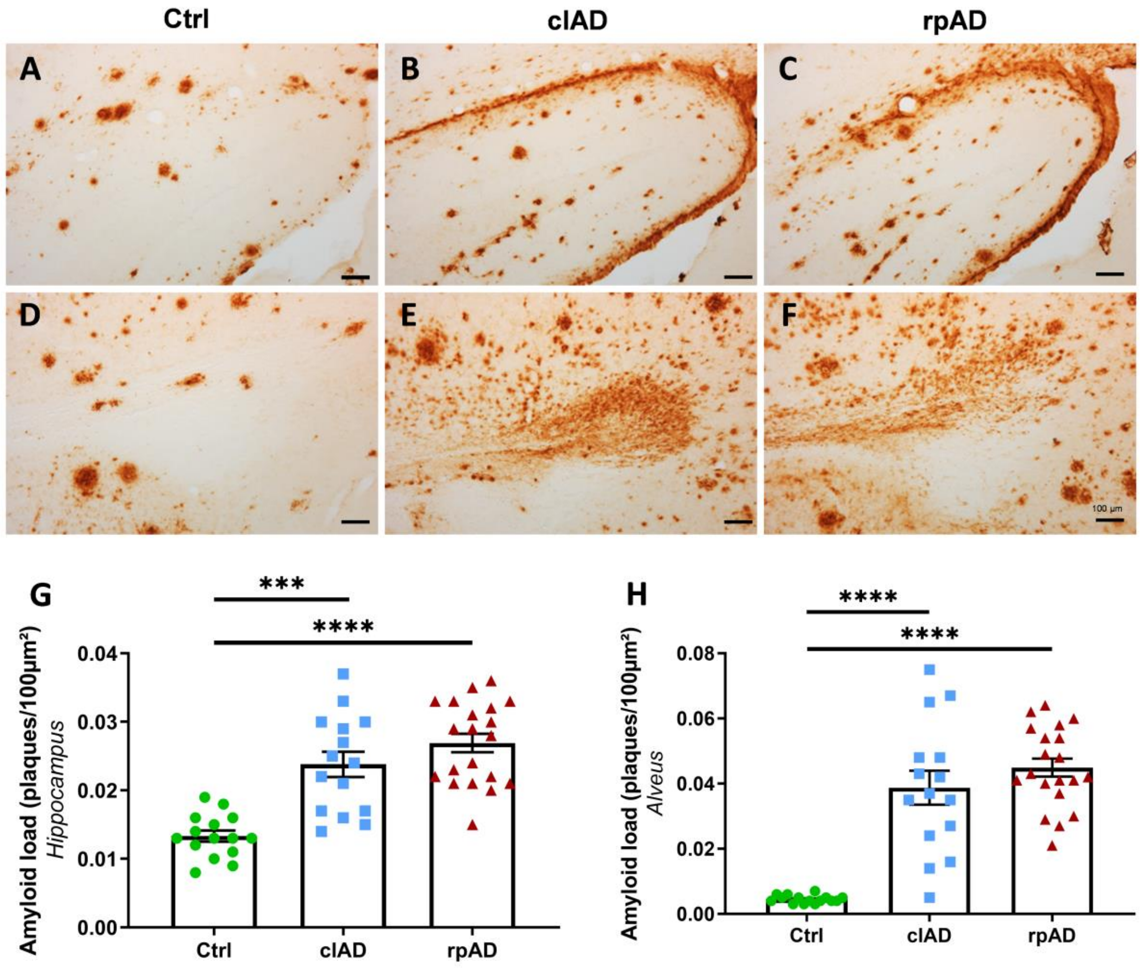

Figure 2. AD brain inoculation accelerates amyloidosis in APP$_{swe}$/PS1$_{dE9}$ mice close to the injection site. (A-F) Representative images of 4G8 immunolabelling showing amyloid pathology in the hippocampus (A-C) and alveus (D-F) of APP$_{swe}$/PS1$_{dE9}$ mice eight months after human brain inoculation. (G-H) Quantification of amyloid load (4G8-positive amyloid plaques per 100 µm²) revealed that AD (clAD and rpAD) brain inoculation accelerates amyloid deposition in the hippocampus (G, p=0.0005 and p<0.0001, respectively) and alveus (H, p<0.0001 and p<0.0001, respectively). Kruskal-Wallis with Dunn's multiple comparisons. ***p<0.001; ****p<0.0001. n$_{Ctrl}$=15, n$_{clAD}$=15, n$_{rpAD}$=20 mice. Data are shown as mean ± s.e.m. Scale bars = 100 µm.

Figure 3

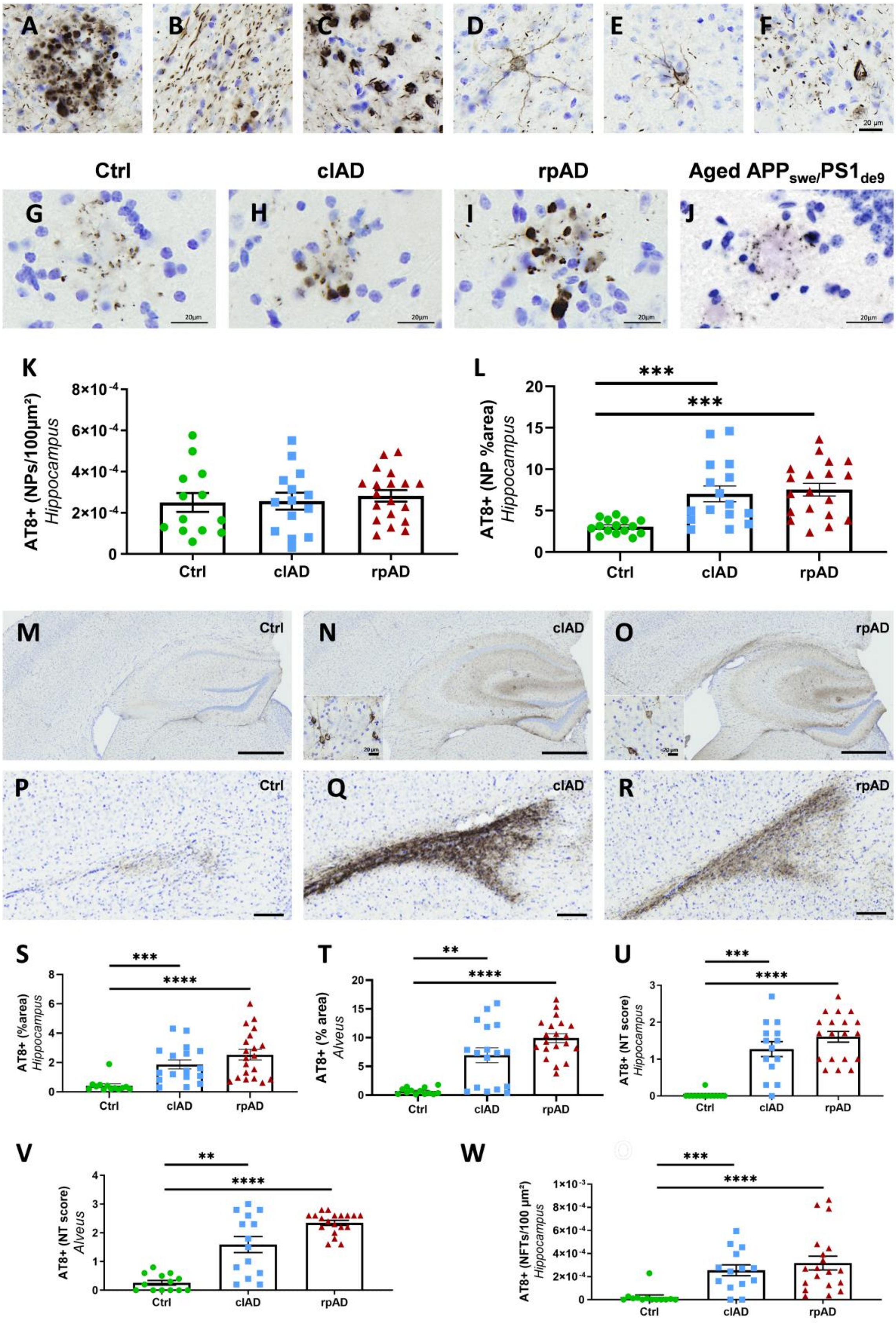
A
B
C
D
E
F
20 µm
Ctrl
cIAD
rpAD
Aged APP$_{swe}$/PS1$_{de9}$
G
H
I
J
20µm
K
AT8+ (NPs/100µm²)
Hippocampus
8×10⁻⁴
6×10⁻⁴
4×10⁻⁴
2×10⁻⁴
0
Ctrl
cIAD
rpAD
L
AT8+ (NP %area)
Hippocampus
***
***
20
15
10
5
0
M
Ctrl
N
cIAD
O
rpAD
20 µm
P
Ctrl
Q
cIAD
R
rpAD
S
AT8+ (%area)
Hippocampus
***
****
8
6
4
2
0
T
AT8+ (% area)
Alveus
**
****
20
15
10
5
0
U
AT8+ (NT score)
Hippocampus
***
****
3
2
1
0
V
AT8+ (NT score)
Alveus
**
****
4
3
2
1
0
W
AT8+ (NFTs/100 µm²)
Hippocampus
***
****
1×10⁻³
8×10⁻⁴
6×10⁻⁴
4×10⁻⁴
2×10⁻⁴
0
Ctrl
cIAD
rpAD

Figure 3. AD brain inoculation induces tau pathology in $\mathbf{APP_{swe}/PS1_{dE9}}$ mice close to the injection site at 8 mpi. AT8 immunolabelling revealed tau lesions in the forms of neuritic plaques (A), neuropil threads (B), neurofibrillary tangles (C-F). Representative images of AT8-positive neuritic plaques within the hippocampus of Ctrl- (G) and AD-inoculated (H for clAD, I for rpAD) mice. AT8 immunolabelling of non-inoculated aged $APP_{swe}/PS1_{dE9}$ mice (24 months old) also revealed neuritic plaques (J). Quantification revealed similar neuritic plaque counts (NPs per 100 µm² of area) in all groups (K). The AT8-positive area within neuritic plaques (NP %area) was higher in AD-inoculated groups compared to Ctrl animals suggesting that neuritic plaques were more tau-positive in AD groups (L, $p=0.001$ and $p<0.0001$, respectively for clAD and rpAD mice, Kruskal-Wallis with Dunn's multiple comparisons). (M-R) Representative images of AT8 immunolabelling showing tau pathology induction in the dorsal hippocampus (M-O) and alveus (P-R). Quantification of overall AT8-labelled phospho-tau (percentage of AT8-positive area), neuropil thread (NT) scoring and/or NFTs accumulation (AT8-positive NFTs per 100 µm² of area) in the hippocampus (S, U, W. S: $p=0.001$ and $p<0.0001$. U: $p=0.0005$ and $p<0.0001$. W: $p=0.001$ and $p<0.0001$, respectively for clAD and rpAD mice; Kruskal-Wallis with Dunn's multiple comparisons) and alveus (T, V. T: $p=0.0035$ and $p<0.0001$. V: $p=0.0036$ and $p<0.0001$, respectively for clAD and rpAD mice; Kruskal-Wallis with Dunn's multiple comparisons) showed an increase in tau pathology following clAD and rpAD brain inoculation compared to Ctrl brain. *$p<0.05$; **$p<0.01$; ***$p<0.001$; ****$p<0.0001$ (Kruskal-Wallis with Dunn's multiple comparisons test). $n_{Ctrl}=15$, $n_{clAD}=15$, $n_{rpAD}=20$ mice. Data are shown as mean ± s.e.m. Scale bars = 20 µm (A-J and inserts), 500 µm (M-O) and 100 µm (P-R).

Figure 4

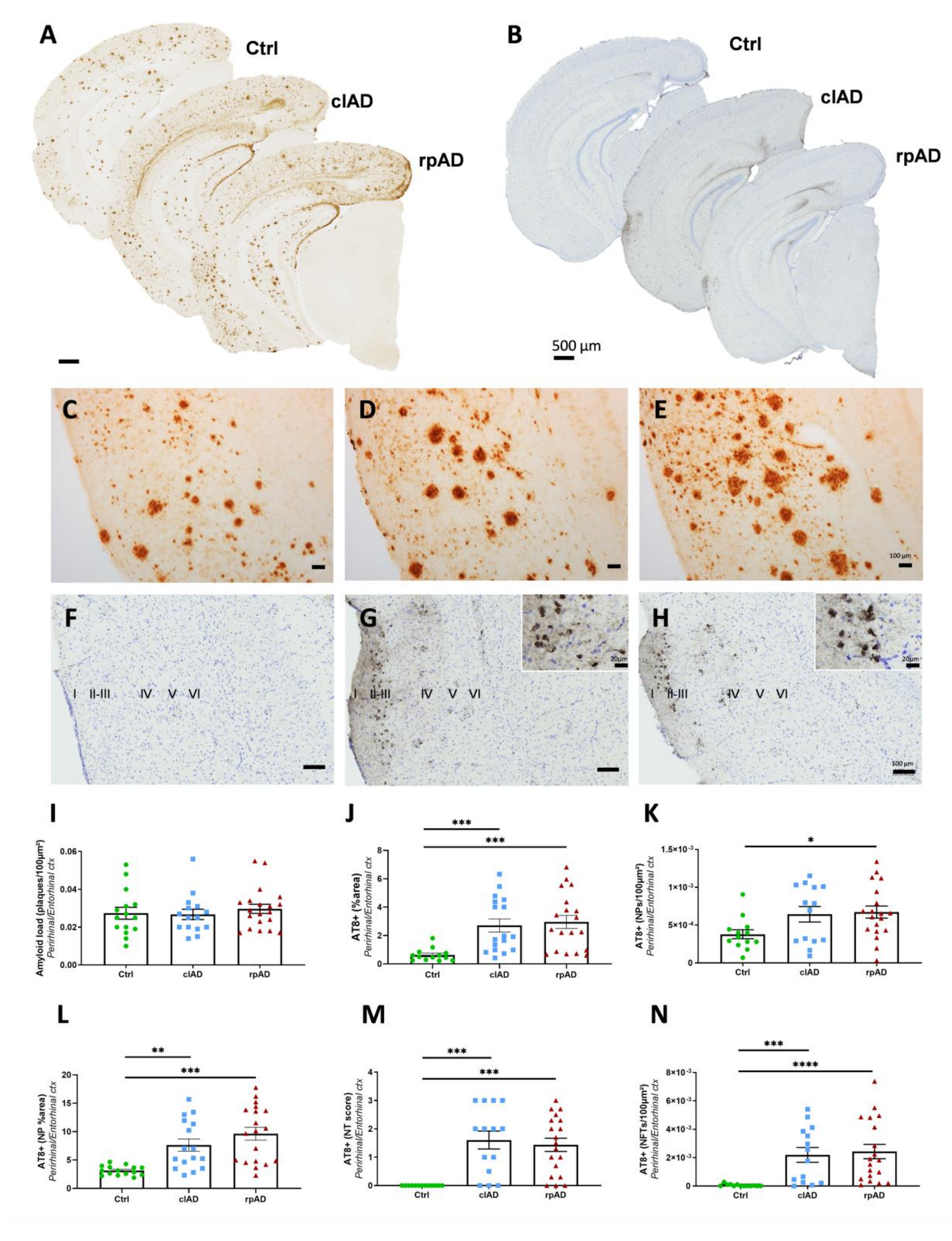

Figure 4. Aβ and tau pathologies in the perirhinal/entorhinal cortex following AD brain inoculation in APP$_{swe}$/PS1$_{dE9}$ mice. Representative images of the 4G8 immunolabelling showing amyloid pathology (A) and the AT8 immunolabelling showing tau pathology (B) in

AD-inoculated $APP_{swe}/PS1_{dE9}$ mice. Magnified views of amyloid (C-E) and tau (F-H) lesions in the perirhinal/entorhinal cortex. Quantification of amyloid load (I: $p>0.05$), overall AT8-positive tau lesions (J: $p=0.0007$ and $p=0.0002$, respectively for clAD and rpAD mice), neuritic plaque (NPs) count (K: $p=0.038$ for rpAD animals versus Ctrl), AT8-positive area stained within neuritic plaques (L: $p=0.0034$ and $p<0.0001$, respectively for clAD and rpAD mice), neuropil thread (NTs – M: $p=0.0003$ and $p=0.0002$, respectively for clAD and rpAD mice), and NFTs (N: $p=0.005$ and $p<0.0001$, respectively for clAD and rpAD mice) in the perirhinal/entorhinal cortex. Kruskal-Wallis with Dunn's multiple comparisons test. ***$p<0.001$; ****$p<0.0001$. $n_{Ctrl}=15$, $n_{clAD}=15$, $n_{rpAD}=20$ mice. Data are shown as mean ± s.e.m. Scale bars = 500 µm (A-B), 100 µm (C-H) and 20 µm in inserts.

Figure 5

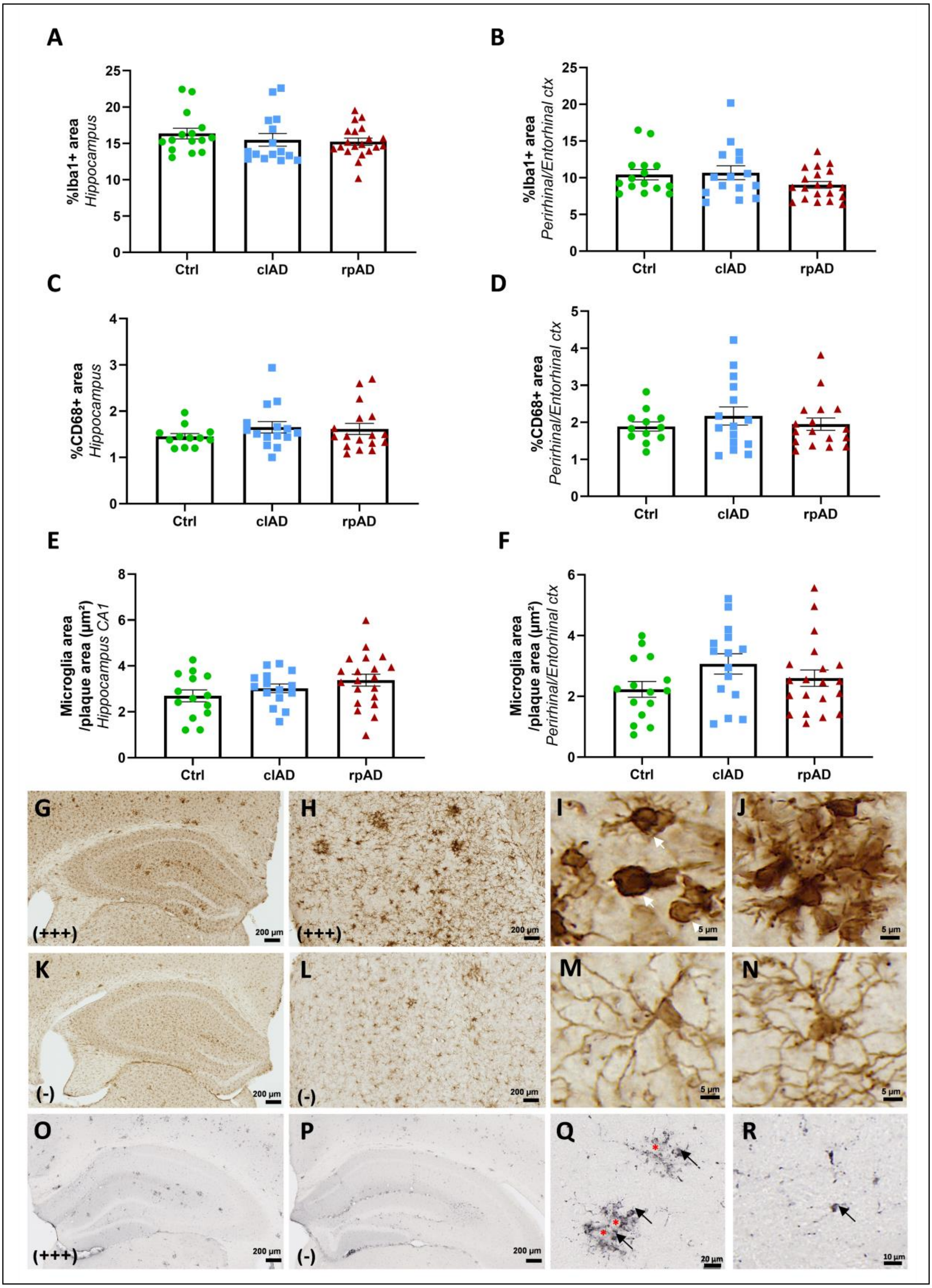
A
%Iba1+ area
Hippocampus
0
5
10
15
20
25
Ctrl
cIAD
rpAD
B
%Iba1+ area
Perirhinal/Entorhinal ctx
0
5
10
15
20
25
Ctrl
cIAD
rpAD
C
%CD68+ area
Hippocampus
0
1
2
3
4
Ctrl
cIAD
rpAD
D
%CD68+ area
Perirhinal/Entorhinal ctx
0
1
2
3
4
5
Ctrl
cIAD
rpAD
E
Microglia area
/plaque area (µm²)
Hippocampus CA1
0
2
4
6
8
Ctrl
cIAD
rpAD
F
Microglia area
/plaque area (µm²)
Perirhinal/Entorhinal ctx
0
2
4
6
Ctrl
cIAD
rpAD
G
(+++)
200 µm
H
(+++)
200 µm
I
5 µm
J
5 µm
K
(-)
200 µm
L
(-)
200 µm
M
5 µm
N
5 µm
O
(+++)
200 µm
P
(-)
200 µm
Q
20 µm
R
10 µm

Figure 5. Microglial activation in AD- and Ctrl-inoculated APP$_{swe}$/PS1$_{dE9}$ mice. Similar levels of Iba1 (A, B) and CD68 (C, D) stained areas in the hippocampus or perirhinal/entorhinal cortex of clAD, rpAD and Ctrl animals (Kruskal-Wallis test). Iba1-positive microglial load surrounding amyloid plaques was also similar in the different groups in both regions (E-F, Kruskal-Wallis test). $n_{Ctrl}=15$, $n_{clAD}=15$, $n_{rpAD}=20$ mice. Within each group, animals with high and low Iba1 staining were identified. Representative images of one animal with higher Iba1 levels showing abundant staining in the hippocampus (G) and perirhinal/entorhinal cortex (H). Animals with higher Iba1 levels displayed activated microglia characterized by beading with spheroidal swellings of the processes and enlarged cell body with dystrophic ramifications (I, arrows). These activated cells formed microglial clusters surrounding Aβ plaques (J). Animals with lower Iba1 levels (K-L) displayed more cells with a highly ramified profile close to amyloid plaques (M) or far from plaques (N), consistent with a non-activated phenotype. (O-P) Representative images of one animal with higher (O) or lower (P) CD68 staining in the hippocampus. (Q-R) Some clusters of CD68-stained microglia (arrows) surrounded amyloid deposits (*) (Q) while some others were not associated with amyloid deposits (R).

Figure 6

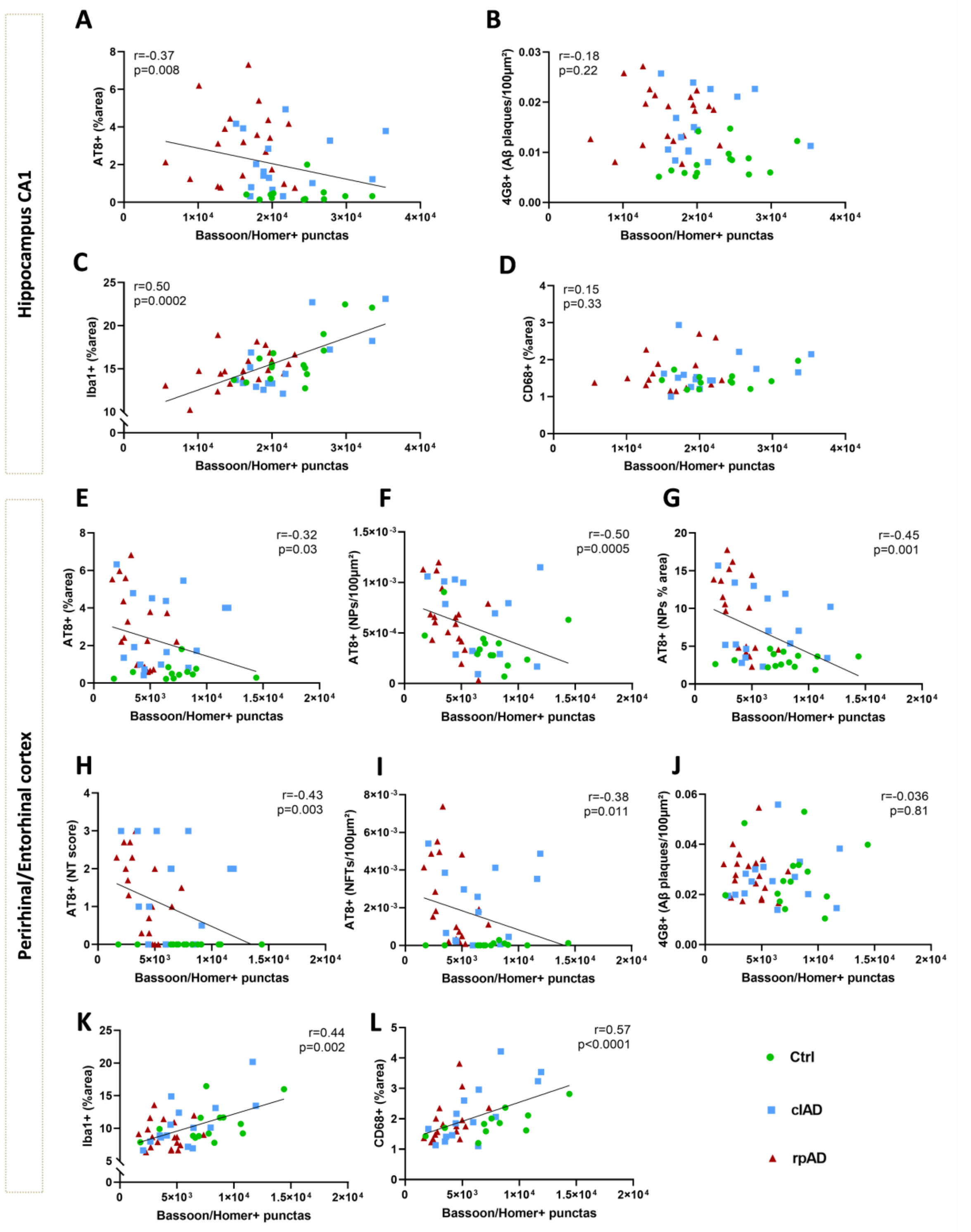

Figure 6. Correlations between synaptic density and tau lesions, Aβ plaque load or microglial activity. Synaptic density (Bassoon/Homer-positive puncta) was negatively correlated with tau pathology both in the hippocampus (CA1) (A) and the perirhinal/entorhinal cortex (E-I), but not with amyloid pathology (B, J). Interestingly,

synaptic density was positively correlated with microglial Iba1 labelling in the hippocampus (C) as well as in the perirhinal/entorhinal cortex (K). Microglial CD68 labelling in the perirhinal/entorhinal cortex (L), but not in the hippocampus (D) was correlated to synaptic density. Spearman's correlations with significance level at $p<0.05$. $n_{Ctrl}=15$, $n_{clAD}=15$, $n_{rpAD}=20$ mice.

Figure 7

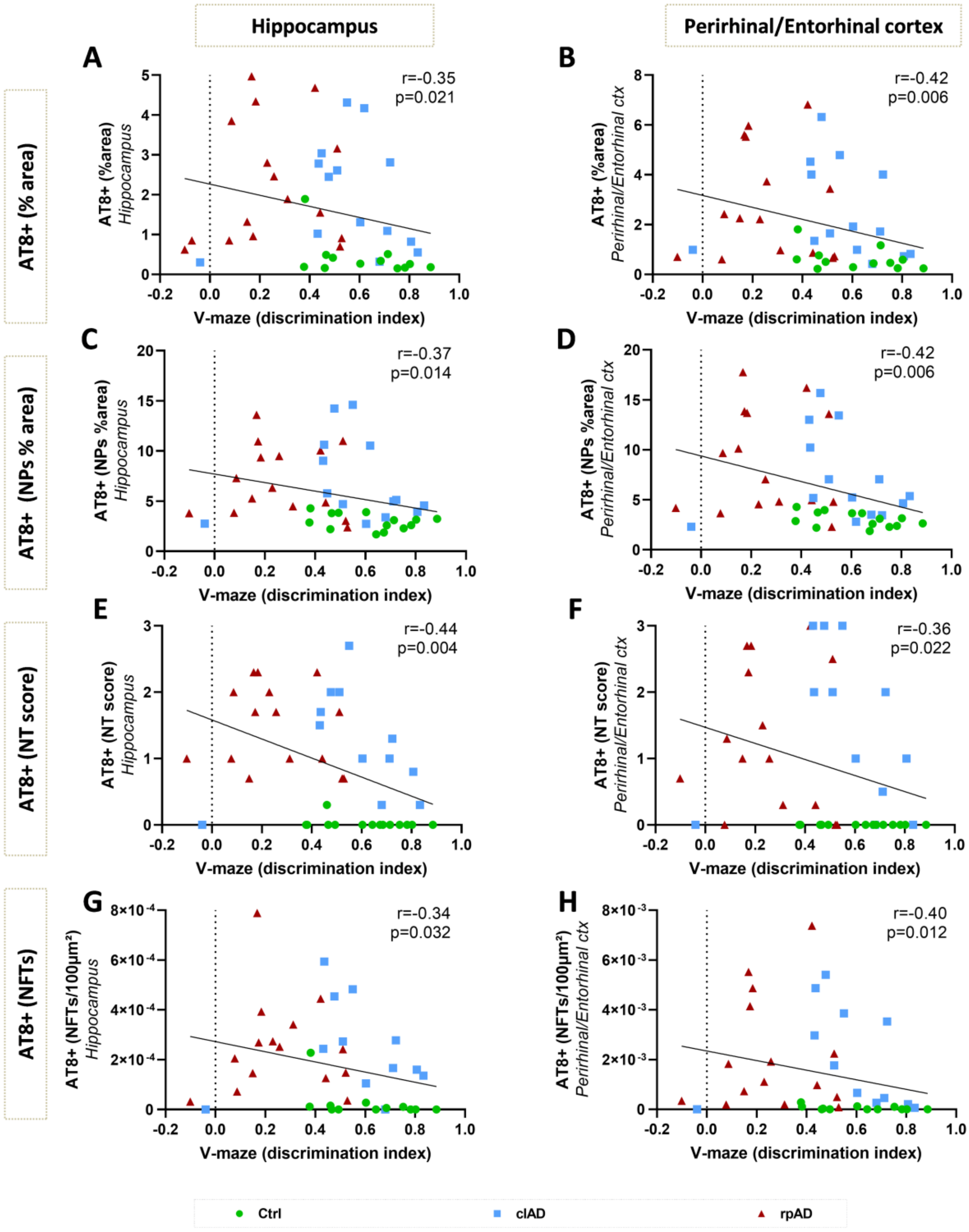

Figure 7. Correlations between V-maze cognitive scores and tau lesions. V-maze cognitive scores (discrimination index) were negatively correlated with tau pathology both in the hippocampus and the perirhinal/entorhinal cortex. (A-B) Overall AT8-positive tau lesions. (C-D) AT8-positive area stained within neuritic plaques. (E-F) Neuropil threads

(NT). (G-H) Neurofibrillary tangles (NFTs). Spearman's correlations with significance level at $p<0.05$. $n_{Ctrl}=15$, $n_{clAD}=15$, $n_{rpAD}=20$ mice.

Figure 8

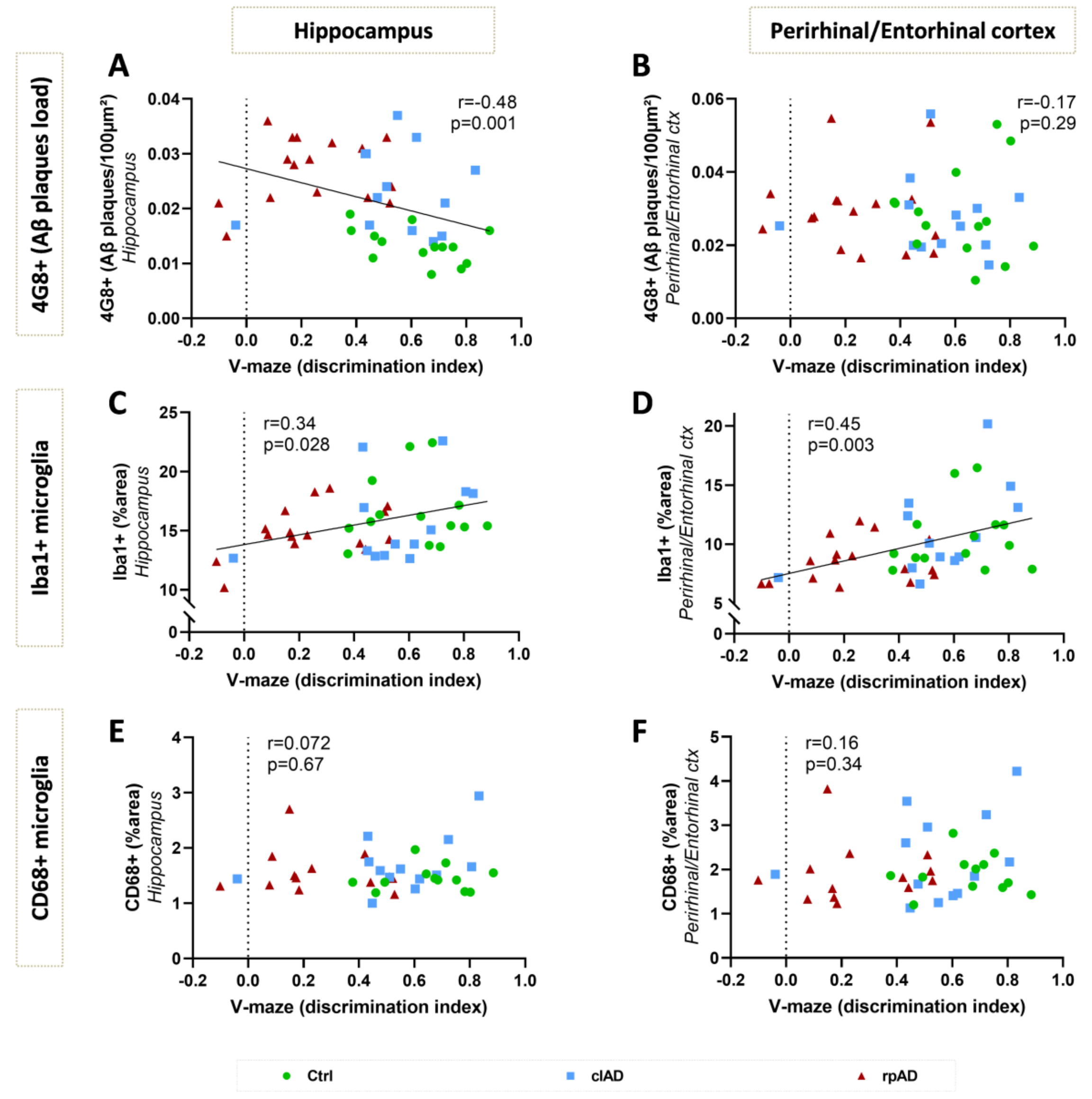

Figure 8. Correlations between V-maze cognitive scores and amyloid or microgliosis. V-maze cognitive scores (discrimination index) were correlated with amyloid pathology in the hippocampus (A) but not in the perirhinal/entorhinal cortex (B). Microglial Iba1-positive staining was positively correlated with cognitive scores in both regions (C-D). Microglial CD68-positive staining was however not correlated with cognitive scores in either region (E-F). Spearman's correlations with significance level at $p<0.05$. $n_{Ctrl}=15$, $n_{clAD}=15$, $n_{rpAD}=20$ mice.

Cognitive, synaptic and neuropathological changes in Alzheimer's brain-inoculated mice

Suzanne Lam, Susana Boluda, Anne-Sophie Hérard, Fanny Petit, Sabiha Eddarkaoui, Karine Cambon, The Brainbank Neuro-CEB Neuropathology Network, Jean-Luc Picq, Luc Buée, Charles Duyckaerts, Stéphane Haïk, Marc Dhenain

Supplementary data

Supplementary Methods

1 Immunohistochemistry of human brain samples

All brain tissues were assessed by immunohistochemistry, as previously described in Gary et al. 2019 (Gary *et al.*, 2019). Briefly, 4-µm-thick paraffin sections were cut, deparaffinized in xylene, successively rehydrated in ethanol (100, 90, and 70%) and rinsed under running tap water for 10 min before immunohistological staining. They were then incubated in 99% formic acid for 5 min, quenched for endogenous peroxidase with 3% hydrogen peroxide and 20% methanol, and washed in water. Sections were blocked at room temperature (RT) for 30 min in 4% bovine serum albumin (BSA) in 0.05 M tris-buffered saline, with 0.05% Tween 20, pH 8 (TBS-Tween, Sigma). They were then incubated overnight at +4 °C with the 6F3D anti-Aβ antibody (Dako, 1/200), polyclonal anti-tau antibody (Dako, 1/500), monoclonal anti-alpha-synuclein (LB509, Zymed, 1/250), polyclonal anti-TDP43 (Protein Tech Group, 1/1000) routinely used for β-amyloid, tau, alpha-synuclein and TDP43 detection, respectively. Sections were further incubated with a biotinylated secondary antibody for 25 min at room temperature, and the presence of the secondary antibody was revealed by a streptavidin–horseradish peroxidase conjugate using diaminobenzidine (Dako, Glostrup, Denmark). Sliced were counterstained with Harris hematoxylin.

2 Characterization of human brain homogenates

Brain homogenates were prepared by combining brain extracts from different patients. clAD and rpAD homogenates consisted in a combination of four brain extracts from the patients with clAD and rpAD, respectively. A third homogenate, considered as a control, was prepared from non-demented individuals (Ctrl, n=2 subjects). These brain homogenates were characterized by biochemistry.

2.1. ELISA quantifications

For amyloid protein quantification, all assay-specific material (pre-coated microtiter plate, buffers, antibodies, standard solutions) was provided in the V-PLEX kit Aβ Peptide Panel 1 (6E10) (MSD®). Human brain homogenates were diluted to 1/5 (Ctrl samples) or 1/10 (clAD and rpAD samples) in the dilution buffer. As described in the manufacturer's protocol, the microtiter plate was blocked for 1 hour at RT with the appropriate buffer. After washing, 25µl of detection antibody and 25µl of diluted sample or standard were added in duplicate to the wells and incubated under continuous agitation for 2h at RT. Wells were washed and 150µl of reading buffer was added. Plate reading was performed with the MSD Sector Imager 2400 (model 1200) multiplex assay system. $A\beta_{1-38}$, $A\beta_{1-40}$ and $A\beta_{1-42}$ quantifications were performed with the Discovery Workbench 4.0 MSD® software.

Tau protein quantifications (total tau (InVitrogen KHB0041) and phosphot-tau181 (InVitrogen KHB00631)) were performed according to the manufacturer’s protocol. Briefly, brain homogenates were diluted to 1/100 and 1/200 in the provided dilution buffer. 50µl of standards or samples, as well as 50µl of detection antibody solution were added to wells and incubated for 14 hours at +4°C. After washing, 100µl of 1X anti-rabbit IgG HRP solution was added for a 30 min incubation period at RT. 100µl of stabilized chromogen were then added to each well for 30 min at RT, in the dark. The reaction was stopped by adding 100µl of Stop solution and the plate was read at 450 nm within the hour. Data were analyzed with GraphPad Prism 7 using the 4PL method. All samples were tested in duplicates.

2.2. Western blots

For tau protein extraction, brain homogenates were sonicated on ice for 5 min, centrifuged for 5 min at 3,000g at +4 °C, diluted in 20 mM Tris/2% SDS and sonicated on ice for 5 min. For tau characterization, samples were diluted to 1 µg/µL, diluted in 2X lithium dodecyl sulfate (LDS, Thermo Fisher Scientific) buffer with reducers and heated at +100 °C for 10 min. 15 µg of samples were loaded on a 12% Bis-TrisCriterion^{TM} gel (Bio-Rad) and migrated in MOPS buffer for 1 hour at 165 V on ice. After protein transfer on nitrocellulose sheets, migration and transfer quality were checked with a ponceau S staining. The membrane was saturated for 1 hour at RT, and was then incubated with the AT100 (pT212-pS214, Life technologies MN1060), 2H9 (pS422, 4BioDx 4BDX-1501), tau-Nter (12-21, LB lab-made) or tau-Cter (clone 9F6, LB lab-made) antibodies overnight at + 4 °C. A peroxidase coupled secondary anti-rabbit or anti-mouse antibody was then applied for 45 min at RT. Immunoblotting was revealed by ECL. GAPDH (Sigma 9545) was used as a loading control. Operators were blinded to the status of the patients.

For Iba1 and GFAP protein extractions, brain homogenates were sonicated (6 strokes, cycle 0.5, 30% amplitude) in a lysis buffer at a final concentration of 50mM Tris-HCl pH 7.4, 150 mM NaCl, 1% Triton-X-100 supplemented with 1X protease inhibitors (cOmplete^{TM} Mini, EDTA-free Protease Inhibitor Cocktail, Roche) and 1/100 diluted phosphatase inhibitors (Phosphatase

Inhibitor Cocktail 2, Sigma-Aldrich). Samples were centrifuged at 20,000g for 20 minutes at +4°C and the supernatant was collected for further use. Extracted samples were stored at -80°C after evaluation of total protein concentration by a BCA assay (Pierce^{TM}). Extracted samples were denatured at +90°C for 5 min in a buffer containing 1X LDS (NuPAGE® LDS sample buffer, Invitrogen) and DTT 1X (NuPAGE® sample reducing agent, Invitrogen). 10 µg of denatured proteins were loaded per well. Samples and the molecular weight marker (Bio-Rad Precision Plus Protein^{TM} Dual Color standards) were loaded on a 4-20% Criterion^{TM} TGX^{TM} gel (Bio-Rad) and migration was performed in a 1X tris-glycine buffer (Bio-Rad) at 120V for 1 hour. Proteins were then transferred to a nitrocellulose membrane using the Trans-Blot® Turbo^{TM} (Biorad) system. Migration and transfer quality were checked with a ponceau S staining. The membrane was then blocked with a TBS/0.1%Tween, 5% milk solution for 1 hour at RT, and incubated with the primary antibody Iba1 (Wako 1919741, 1/2000), GFAP (Dako Z0334, 1/5000) or actin (Sigma A2066, 1/5000) diluted in saturation buffer overnight at +4°C. After washing in TBS/0.1% Tween solution, the membrane was incubated with the appropriate secondary HRP-conjugate antibody diluted to 1/5000 in TBS/0.1%Tween for 1h at RT. The chemiluminescent signal was revealed using the Clarity western ECL (Bio-Rad) kit and the Chemidoc^{TM} MP (Bio-Rad) imaging system. Protein band intensities were quantified on the ImageJ software and normalized by actin expression levels.

3 Stereotaxic surgery

Two month-old $APP_{swe}/PS1_{dE9}$ and wild-type littermates were anesthetized by an intraperitoneal injection of ketamine (1mg/10g; Imalgène 1000, Merial) and xylazine (0.1mg/10g; 2% Rompun, Bayer Healthcare). Local anesthesia was also performed by a subcutaneous injection of lidocaine at the incision site (1 µl/g; 0.5% Xylovet, Ceva). Mice were placed in the stereotaxic frame (Phymep) and bilateral injections of brain samples were performed in the dorsal hippocampus (AP

-2 mm, DV -2 mm, L +/- 1 mm from bregma). Using 34-gauge needles and Hamilton syringes, 2µl of sample were administered at a 0.2µl/min rate. After the injection, needles were kept in place for 5 more minutes before removal and the incision was sutured. The surgical area was cleaned before and after the procedure using povidone iodine (Vétédine, Vétoquinol). Respiration rate was monitored and body temperature was maintained at 37±0.5°C with a heating pad during the surgery. Anesthesia was reversed with a subcutaneous injection of atipamezole (0.25 mg/kg; Antisedan, Vetoquinol). Mice were placed in a ventilated heating box (25°C) and monitored until full recovery from anesthesia. Postoperative pain management consisted in paracetamol administration in drinking water (1.45ml/20ml of water; Doliprane, Sanofi) during 48 hours.

4 Behavioral evaluations

Mice were studied using an elevated plus maze, a novel object recognition task in a V-maze, and a Morris water maze. Between each mice, the elevated plus maze and V-maze were cleaned with 10% ethanol and dried. Performances were recorded using a tracking software (EthoVision XT14, Noldus).

4.1. Elevated plus maze

The elevated plus maze is a plus-shaped apparatus placed at 50 cm above the floor. It consists in four 5 cm-wide and 40 cm-long segments, among which two are open arms (associated with a 150 lux-lighting) and two are enclosed arms (associated with a 15 lux-lighting). Mice were placed at the center of the maze facing an open arm for a 6-min trial. Distance travelled and time spent in each arm were automatically calculated by the software. The time spent leaning over the edge of open arms was scored manually.

4.2. Novel object recognition in the V-maze

The V-maze arena consisted in two 6 cm-wide, 33.5 cm-long and 15 cm-high black arms forming a V shape and exposed to a 50 lux-lighting. The test was divided into three phases, each one separated by 24 hours. At the beginning of each session, mice were placed at the center of the arena, *i.e.* at the intersection of the arms. During the habituation phase (day 1), mice were free to explore the empty arena for 9 minutes. The distance travelled was automatically recorded as an indicator of their exploratory activity. For the training phase (day 2), two identical objects (bicolor plastic balls) were placed at the end of each arm. Exploratory activity was evaluated as the time spent exploring the objects (manually recorded) and the distance travelled during the 9-minute trial. On the test day (day 3), one familiar object (a bicolor plastic ball) was replaced by a novel one of a different shape and material (a transparent glass flask). Recognition was assessed using a discrimination index, calculated as follows:

$$Discrimination\ index = \frac{Time\ exploring\ the\ novel\ object - Time\ exploring\ the\ familiar\ object}{Total\ exploration\ time}$$

It reflects the time spent exploring each object, and therefore, the ability to discriminate a novel object from a familiar, previously explored one. A high discrimination index score reveals that mice spent more time exploring the new object, *i.e.* had less interest in a familiar object, and suggests that their memory is not impaired.

4.3. Morris water maze

An open 122 cm-wide circular swimming arena was maintained at 22°C and exposed to a 400 lux-lighting. The test consisted of three phases during which the arena was divided into four artificial quadrants. At the end of each session, mice were dried with a heated towel before returning to their home cages. During the habituation phase (day 1), mice were trained to find a visible platform to escape from the water. To facilitate its detection, the platform was emerged 0.5 cm above the surface of the water and a colorful cue was placed on it. This phase consisted in four 60-seconds trials, with an inter-trial interval (ITI) of 20-30 minutes. For each trial, the starting point was different as well as the location of the platform. When the mice did not find the platform within the 60 seconds, they were guided to its location and were left on the plateform to rest for 30 seconds. The training phase (day 2 to 6) consisted in three daily 60-seconds trials, with 20-30 minutes ITI, for five days. For each trial, the starting point was different whereas the location of the platform remained the same. The platform was hidden 0.5 cm beneath the water surface and the cue previously placed on it was removed. Visual cues were placed around the maze so that mice could spatially navigate to the platform. When the mice did not find the platform within the 60 seconds, they were guided to its location and were left on the platform to rest for 30 seconds. All trials lasted 60 seconds or until the animal located the platform. Escape latency, *i.e.* the time required to find the platform, was evaluated during the habituation and the training phases to assess learning abilities. A probe test (day 7) was performed 72 hours after the last training session to assess spatial long-term memory. During this phase, the platform was removed from the maze. Mice were placed in the water for 60 seconds from a position opposite to the platform. The time spent in each virtual quadrant of the maze was recorded.

5 Immunohistochemistry for amyloid, tau, microgliosis, and astrogliosis

Amyloid deposits were evaluated using a 4G8 labelling. Tau was evaluated using AT8 and AT100 labellings. Microgliosis was evaluated using Iba1 and CD68 antibodies. Astrocytes were stained using a GFAP antibody. 4G8 labelling was performed after pretreating brain sections with 70% formic acid (VWR®) for 20 min at RT. AT8 and AT100 labellings were performed after a pretreatment with EDTA 1X citrate (Diagnostic BioSystems®) for 30 min at 95°C. All tissues were then incubated in hydrogen peroxide H_2O_2 30% (Sigma-Aldrich®) diluted 1/100 for 20 min to inhibit endogenous peroxidases. Blocking of non-specific antigenic sites was achieved over 1 hour using a 0.2% Triton X-100/0.1M PBS (Sigma-Aldrich®) (PBST) solution containing 4.5% normal goat serum or 5% bovine serum albumin. Sections were then incubated at +4°C with the 4G8 (Biolegend 800706, 1/500), Iba1 (Wako 1919741, 1/1000), CD68 (Serotec – Biorad MCA 1957, 1/800) or GFAP (Dako Z0334, 1/10000) antibody diluted in a 3%NGS/PBST solution for 48h, or with the AT8 (Thermo MN1020B, 1/500) or AT100 (Thermo MN1060, 1/500) antibody diluted in a 3%NGS/PBST solution for 96h. After rinsing, an incubation with the appropriate biotinylated secondary antibody diluted to 1/1000 in PBST was performed for 1h at RT, followed by a 1h incubation at room temperature with a 1:250 dilution of an avidin-biotin complex solution (ABC Vectastain kit, Vector Laboratories®). Revelation was performed using the DAB Peroxidase Substrate Kit (DAB SK4100 kit, Vector Laboratories®). Sections were mounted on Superfrost Plus slides (Thermo-Scientific®). For the AT8 and AT100 labellings, a cresyl violet counterstain was performed. All sections were then dehydrated in successive baths of ethanol at 50°, 70°, 96° and 100° and in xylene. Slides were mounted with the Eukitt® mounting medium (Chem-Lab®).

Stained sections were scanned using an Axio Scan.Z1 (Zeiss® - Z-stack images acquired at 20× (z-stacks with 16 planes, 1µm steps with extended depth of focus)). Each slice was extracted individually in the .czi format using the Zen 2.0 (Zeiss®) software. Image processing and analysis were performed with the ImageJ software. Macros were developed for each staining in order to achieve a reproducible semi-automated quantification. Images were imported with a 50% reduction in resolution (0.44 µm/pixel), converted to the RGB format and compressed in .Tif format. For the 4G8, Iba1 and CD68 immunostainings, segmentation was performed through an automatic local thresholding using the Phansalkar method (radius=15). Amyloid load was evaluated after quantification of the 4G8-labelled particles between 8 and 2,000 µm², and normalization to the surface area of each ROI. Microglial activity was evaluated as a percentage of Iba1- or CD68-positive surface area in each ROI. For the AT8 and AT100 stainings, the blue component of each image was extracted in order to remove the cresyl violet counter-staining from the analysis. An automatic local thresholding of the staining was carried out with the Phansalkar method and the severity of tau pathology was evaluated as a percentage of AT8-positive or AT100-positive surface area in each ROI. In addition for the AT8 immunostaining, a quantification of neuritic plaques and AD-like neurofibrillary tangles was performed by manual counting. The AT8-positive area stained within neuritic plaques was evaluated by drawing circular regions of interest (with a constant area of 6µm²), and by quantifying the percentage of tau-positive regions within each ROI, using the same thresholding method as previously described. A semi-quantitative analysis of neuropil threads was also performed by assigning a severity score based on the intensity and extent of AT8-positive staining in each ROI. All quantifications were performed on adjacent slices between -0.34 mm and -4.36 mm from bregma. Ten adjacent slices were analyzed for the 4G8 staining, and 5 for Iba1, CD68, AT8, and AT100 stainings. All ROIs were manually segmented using the Paxinos and Franklin Neuro-Anatomical Atlas of Mouse Brain (Paxinos and Franklin, 2001).

6. Gallyas silver staining

Free-floating sections were mounted on Superfrost Plus (Thermo-Scientific®) slides and dried overnight prior to Gallyas staining. Section were permeabilized by successive incubations in toluene (2x5min) followed by ethanol at 100°, 90° and 70° (2 min per solution). Slides were then incubated in a 0.25% potassium permanganate solution for 15 min, in 2% oxalic acid for 2 min then in a lanthanum nitrate solution (0.04g/l lanthanum nitrate, 0.2g/l sodium acetate, 10% H_2O_2 30%) for 1h to reduce non-specific background. Several rinses with distilled water were performed followed by an incubation in an alkaline silver iodide solution (3.5% $AgNO_3$ 1%, 40g/l NaOH, 100g/l KI) for 2 min. The reaction was neutralized with 0.5% glacial acetic acid baths (3x1min) and sections were incubated for 20 min in a developing solution (2g/l NH4NO3, 2g/l AgNO3, 10g/l tungstosilicilic acid, 0.76% formaldehyde 37%, 50g/l anhydrous Na2CO3). Several rinses with 0.5% acetic acid (3x1min) followed by an incubation in 1% gold chloride solution for 5min were then carried out. Sections were rinsed with distilled water and the staining was fixed with a 1% sodium thiosulfate solution. All sections were then rinsed with distilled water and dehydrated for 1 to 5 min in successive baths of ethanol at 50°, 70°, 96° and 100° and in xylene. Slides were mounted with the Eukitt® mounting medium (Chem-Lab®). All steps were performed between 20 and 25°C.

7. Co-staining of microglia and amyloid plaques

In order to evaluated microglial load surrounding amyloid plaques, the co-staining of microglia and amyloid plaques was performed. Free-floating sections were permeabilized in a 0.2% Triton X-100/0.1M PBS (Sigma-Aldrich®) solution for 3x10min. Slices were stained by MXO4 dye (Tocris #4920, 1/300) for 30 min at RT, and then washed in a 0.1M PBS solution. Sections were blocked in a 4.5%NGS/PBST solution for 1h at RT before being incubated with the Iba1 antibody (Wako 1919741, 1/1000). On the next day, sections were rinsed in 0.1M PBS and incubated for 1h at RT with the appropriate secondary antibody diluted to 1/1000 in PBST (anti-rabbit AlexaFluor 633). Sections were rinsed and mounted on Superfrost Plus (Thermo-Scientific®) slides with the Vectashield® mounting medium with a refractive index of 1.45. Images of stained sections were acquired using a Leica DMI6000 confocal optical microscope (TCS SPE) with a 40x oil-immersion objective (refractive index 1.518) and the Leica Las X software. A confocal zoom of 3 and a pinhole aperture fixed at 1 Airy were applied. Acquisition was performed in sequential mode with a sampling rate of 1024x1024 and a scanning speed of 700 Hz. Image resolution was 60 nm/pixel and the optical section was 0.896 µm. 12 separate planes with a 0.1 µm step were acquired. The excitation wavelengths were 633 nm (for Iba1) or 350 nm (for Aβ). Image acquisition was performed on 2 slices located between -3.28 mm and -4.24 mm from the bregma, with 3 images per slice for the CA1 region and for the perirhinal/entorhinal cortex. 3D deconvolution of the images was performed using the AutoQuant X3 software. The deconvoluted 8-bit images were analyzed using the ImageJ software. Quantification of microglial load around plaques was based on a thresholding procedure applied across all images to segment microglial cells. MXO4-positive surfaces were dilated as circular regions of interest (with a diameter of 40 µm) were drawn around the amyloid plaque to define a dilated plaque area. Microglial staining within the dilated surface, *e.g.* within the plaque area, was included in the analysis.

References

Gary C, Lam S, Herard AS, Koch JE, Petit F, Gipchtein P, *et al.* Encephalopathy induced by Alzheimer brain inoculation in a non-human primate. Acta Neuropathol Commun 2019; 7(126).

Paxinos G, Franklin KBJ. The mouse brain in stereotaxic coordinates. second ed. San Diego: Academic Press; 2001.

Supplementary Tables

Supplementary Table 1

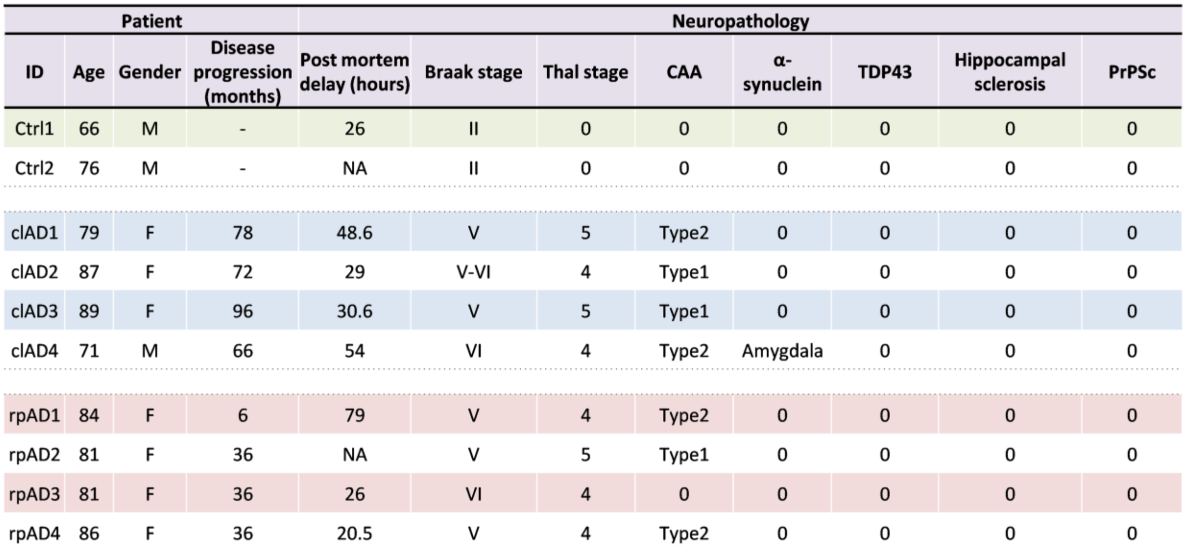

Patient				Neuropathology							
ID	Age	Gender	Disease progression (months)	Post mortem delay (hours)	Braak stage	Thal stage	CAA	α-synuclein	TDP43	Hippocampal sclerosis	PrPSc
Ctrl1	66	M	-	26	II	0	0	0	0	0	0
Ctrl2	76	M	-	NA	II	0	0	0	0	0	0
clAD1	79	F	78	48.6	V	5	Type2	0	0	0	0
clAD2	87	F	72	29	V-VI	4	Type1	0	0	0	0
clAD3	89	F	96	30.6	V	5	Type1	0	0	0	0
clAD4	71	M	66	54	VI	4	Type2	Amygdala	0	0	0
rpAD1	84	F	6	79	V	4	Type2	0	0	0	0
rpAD2	81	F	36	NA	V	5	Type1	0	0	0	0
rpAD3	81	F	36	26	VI	4	0	0	0	0	0
rpAD4	86	F	36	20.5	V	4	Type2	0	0	0	0

Supplementary Table 1. Patient characteristics. Age-matched classical (clAD) and rapidly evolving (rpAD) AD patients were selected based on disease duration (over or under 36 months) and neuropathological evaluation, including similar Braak and Thal stages. Brains were negative for α-synuclein, TAR DNA-binding protein 43 (TDP43), hippocampal sclerosis and pathological prion PrPSc. Two non-AD control individuals (Ctrl) were also included in this study. NA: not available.

Supplementary Table 1

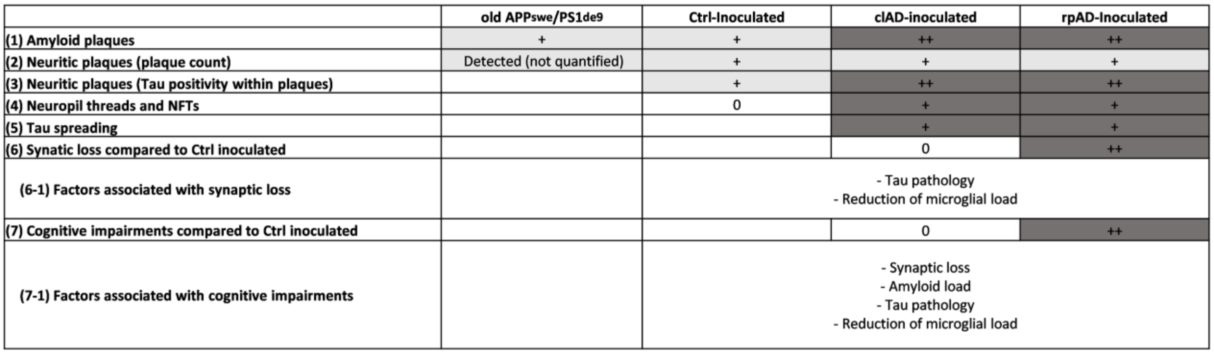

	old APP$_{swe}$/PS1$_{de9}$	Ctrl-Inoculated	clAD-inoculated	rpAD-Inoculated
(1) Amyloid plaques	+	+	++	++
(2) Neuritic plaques (plaque count)	Detected (not quantified)	+	+	+
(3) Neuritic plaques (Tau positivity within plaques)		+	++	++
(4) Neuropil threads and NFTs		0	+	+
(5) Tau spreading			+	+
(6) Synatic loss compared to Ctrl inoculated			0	++
(6-1) Factors associated with synaptic loss		- Tau pathology - Reduction of microglial load		
(7) Cognitive impairments compared to Ctrl inoculated			0	++
(7-1) Factors associated with cognitive impairments		- Synaptic loss - Amyloid load - Tau pathology - Reduction of microglial load		

Supplementary Table 2. Overview of the results of this study. The study focused on Aβ plaque-bearing APP$_{swe}$/PS1$_{dE9}$ mice (1). Old mice and mice inoculated with Ctrl-human brain extract presented with tau-positive neuritic plaques (2). Inoculation of AD-brain extracts increased tau positivity within neuritic plaques (3) and induced neuropil threads and NFTs in inoculated mice (4). Tau lesions spread in regions connected to the inoculation site (5). Synaptic (6) and cognitive impairments (7) were detected in animals inoculated with brains from patients with a rapidly evolving form of AD (rpAD). Synaptic loss was associated with tau pathologies and a reduction of activated microglial load (6-1). Cognitive impairments were associated with synaptic loss, with amyloid and tau loads, and to a lesser extent with a reduction of activated microglial load (7-1).

Supplementary Figures

Supplementary Figure 1

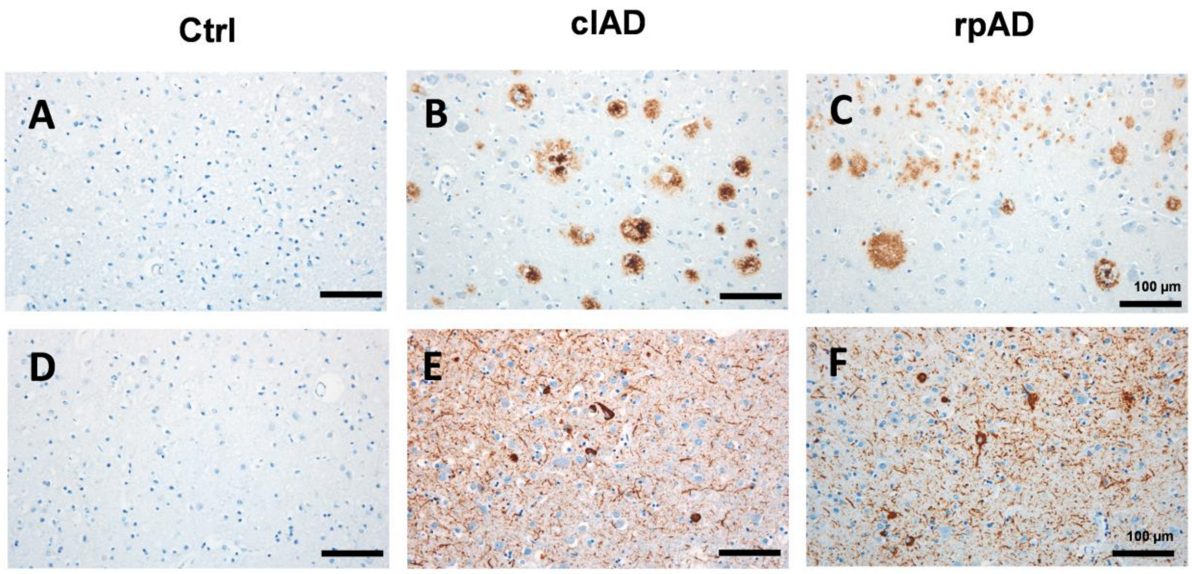

Supplementary Figure 1. Amyloid and tau pathological evaluations in human brain samples. Representative images of Ctrl, clAD and rpAD brain samples stained for amyloid (A-C, 6F3D anti-Aβ antibody) and tau (D-F, polyclonal anti-tau antibody) pathologies. Scale bars = 100 µm.

Supplementary Figure 2

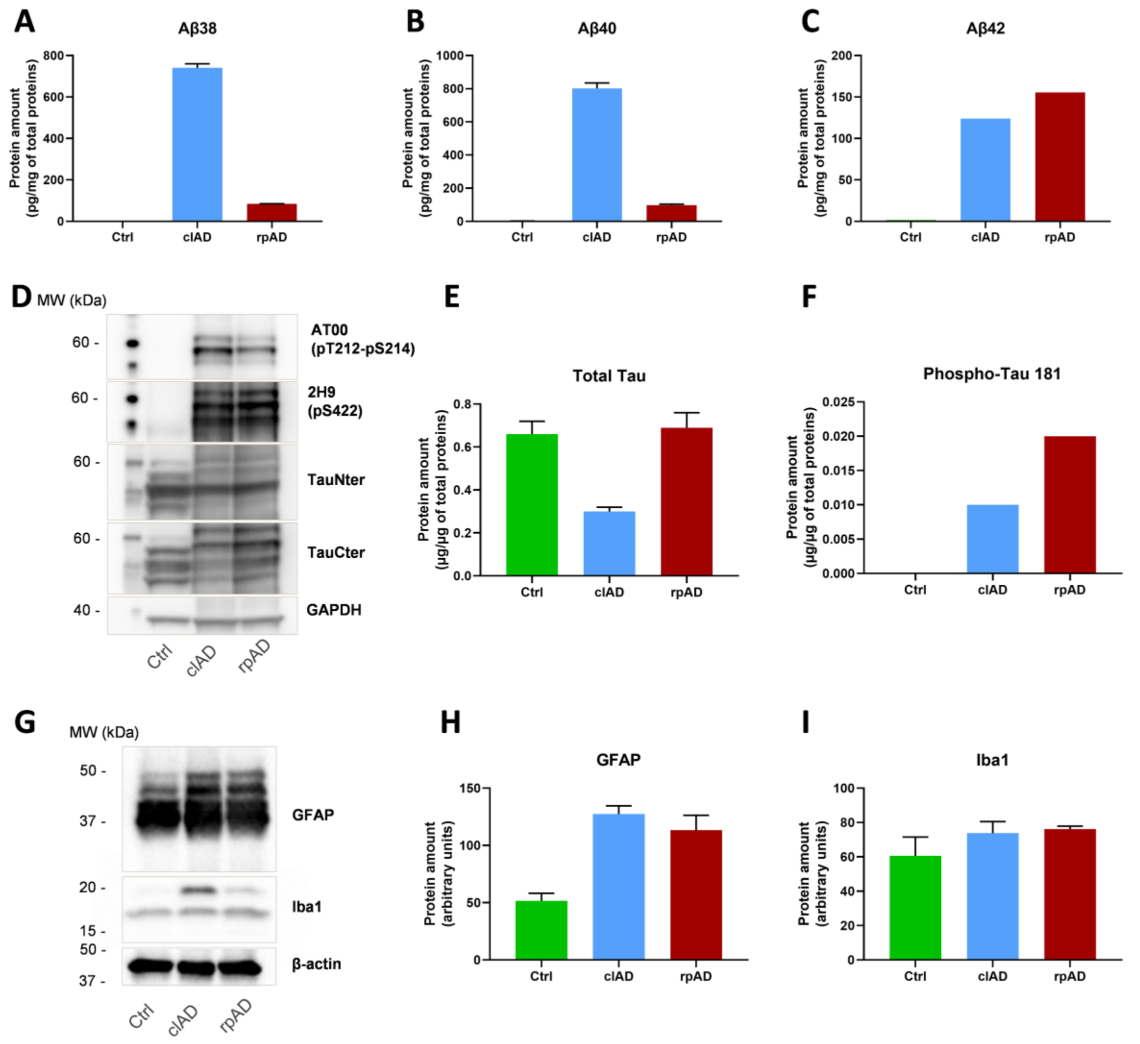

Supplementary Figure 2. Biological characteristics of brain homogenates inoculated to animals. Three brain homogenates were prepared from the 2 Ctrl, 4 clAD and 4 rpAD cases (Ctrl, clAD and rpAD homogenates respectively). All quantifications of the inoculated brain homogenates (Ctrl, clAD or rpAD) were performed in duplicate and data are shown as mean ± standard deviation of the replicates. (A-C) Quantifications of total Aβ_{38}, Aβ_{40} and Aβ_{42} of the inoculated brain extracts (MSD technology). Both AD inocula had more Aβ proteins compared to the Ctrl one. The clAD inoculum showed more Aβ_{38} and Aβ_{40} than the rpAD one. (D-F) Tau profile evaluation revealed a pathological hyperphosphorylated tau triplet at 60, 64 and 69 kDa observed in AD and a typical shift in the molecular weight of the Alzheimer Tau-Cter triplet in western blots (D). Total tau (E) and pathological phospho-tau 181 levels (F) were assessed using ELISA quantifications. (G-I) Neuroinflammatory profile evaluation by western blots revealed higher astrocytic presence (GFAP-positive) in clAD and rpAD inocula compared to the Ctrl extract (G-H). Microglial (Iba1-positive) levels were similar in the Ctrl, clAD and rpAD groups (G, I).

Supplementary Figure 3

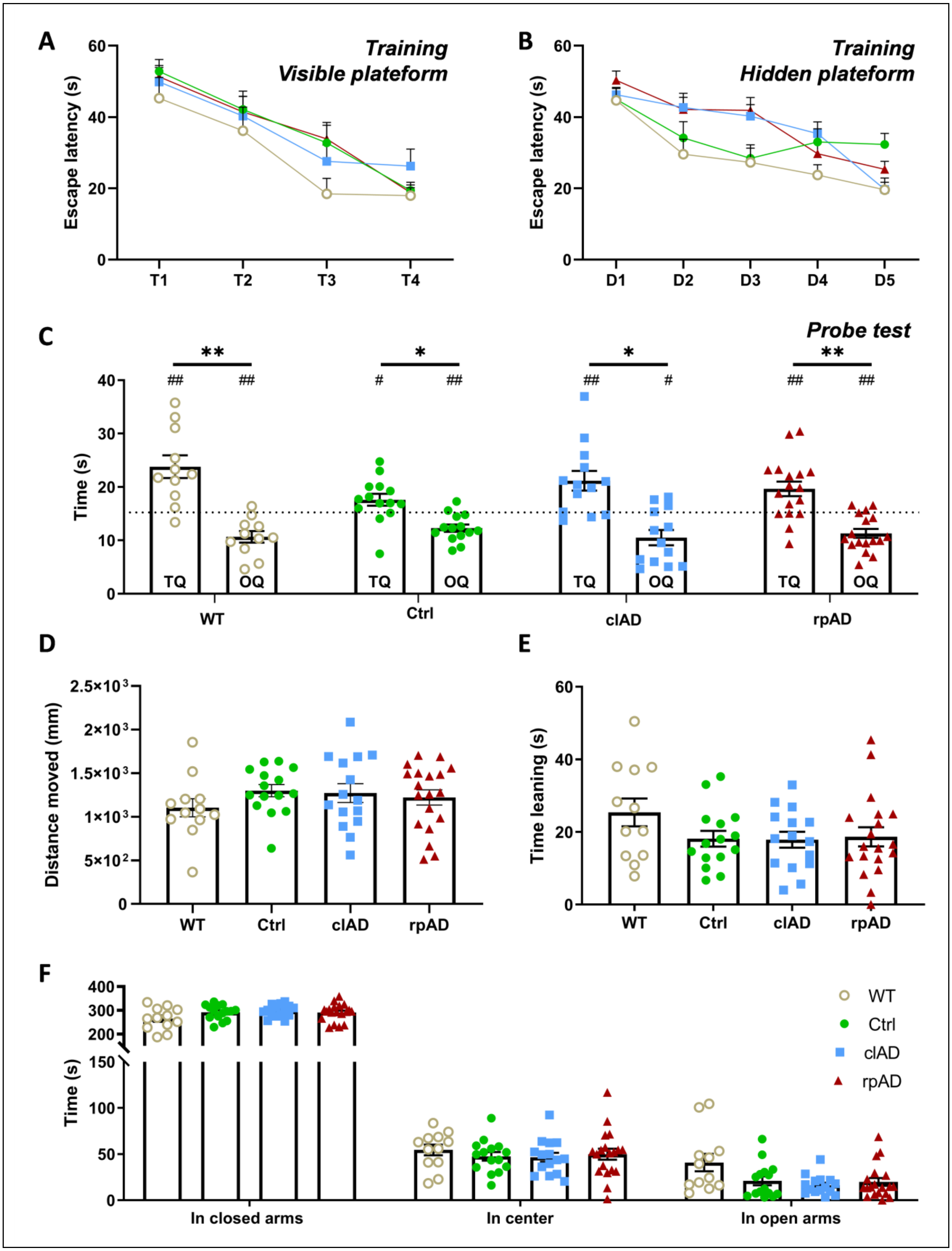

Supplementary Figure 3. Inoculated mice showed similar spatial memory performances and anxiety levels at 8 mpi. (A-C) Spatial memory was assessed using the Morris water maze test. During the visible platform phase (A), escape latencies steadily decreased across the four trials ($F_{(2.649,\ 135.1)} = 36.67$, $p<0.0001$; two-way repeated measures ANOVA with the Geisser-Greenhouse correction and Dunnett's multiple comparisons). No difference was observed between the groups ($F_{(3,\ 51)}=1.87$, $p=0.15$; two-way repeated measures ANOVA with the Geisser-Greenhouse correction and Dunnett's multiple comparisons). For the hidden platform training phase (B), escape latencies were averaged across three trials per day and slowly decreased across the trials and days suggesting that mice had successfully learnt the platform position ($F_{(3.575,\ 182.3)} = 36.09$, $p<0.0001$; two-way repeated measures ANOVA with the Geisser-Greenhouse correction and Dunnett's multiple comparisons). No difference was observed between the groups suggesting that Ctrl, clAD and rpAD brain inoculations do not differentially impact spatial learning abilities in $APP_{swe}/PS1_{dE9}$ mice after an eight-month incubation period ($F_{(2,\ 41)}=0.85$, $p=0.88$; two-way repeated measures ANOVA with the Geisser-Greenhouse correction and Dunnett's multiple comparisons). During the probe test evaluating spatial memory (C), the time spent in the target quadrant (TQ) was significantly higher than the time spent in the opposite one (OQ) (*$p<0.05$ for Ctrl and clAD-inoculated $APP_{swe}/PS1_{dE9}$ mice or **$p<0.01$ for WT mice and rpAD-inoculated $APP_{swe}/PS1_{dE9}$ mice; two-way repeated measures ANOVA with the Geisser-Greenhouse correction and Dunnett's multiple comparisons). Moreover, the time spent both in the TQ and OQ was significantly different from 15 seconds, which corresponds to 25% of the trial duration (# $p<0.05$; one-sample Wilcoxon's signed-rank test). Spatial memory retention was evaluated after 72 hours. All groups performed as well as the WT group by spending more time in the target quadrant than in the opposite one, suggesting that memory is not impaired in $APP_{swe}/PS1_{dE9}$ Ctrl or AD-inoculated mice (for the groups: $F_{(3,\ 51)} = 0.83$, $p>0.05$; for TQ versus OQ: $p=0.0028$, 0.0217, 0.0117 and 0.0013, respectively for Wt, Ctrl, clAD and rpAD groups; two-way ANOVA with the Geisser-Greenhouse correction and Dunnett's multiple comparisons). (D-F) Anxiety levels were assessed using the elevated plus maze. Comparable travelled distance (D), time spent leaning over the maze (E) and time spent in the different areas of the maze (open/closed arms and center of the maze) (F) were reported between the groups ($p>0.05$; Kruskal-Wallis' test with Dunn's multiple comparisons). Data are shown as mean ± s.e.m.

Supplementary Figure 4

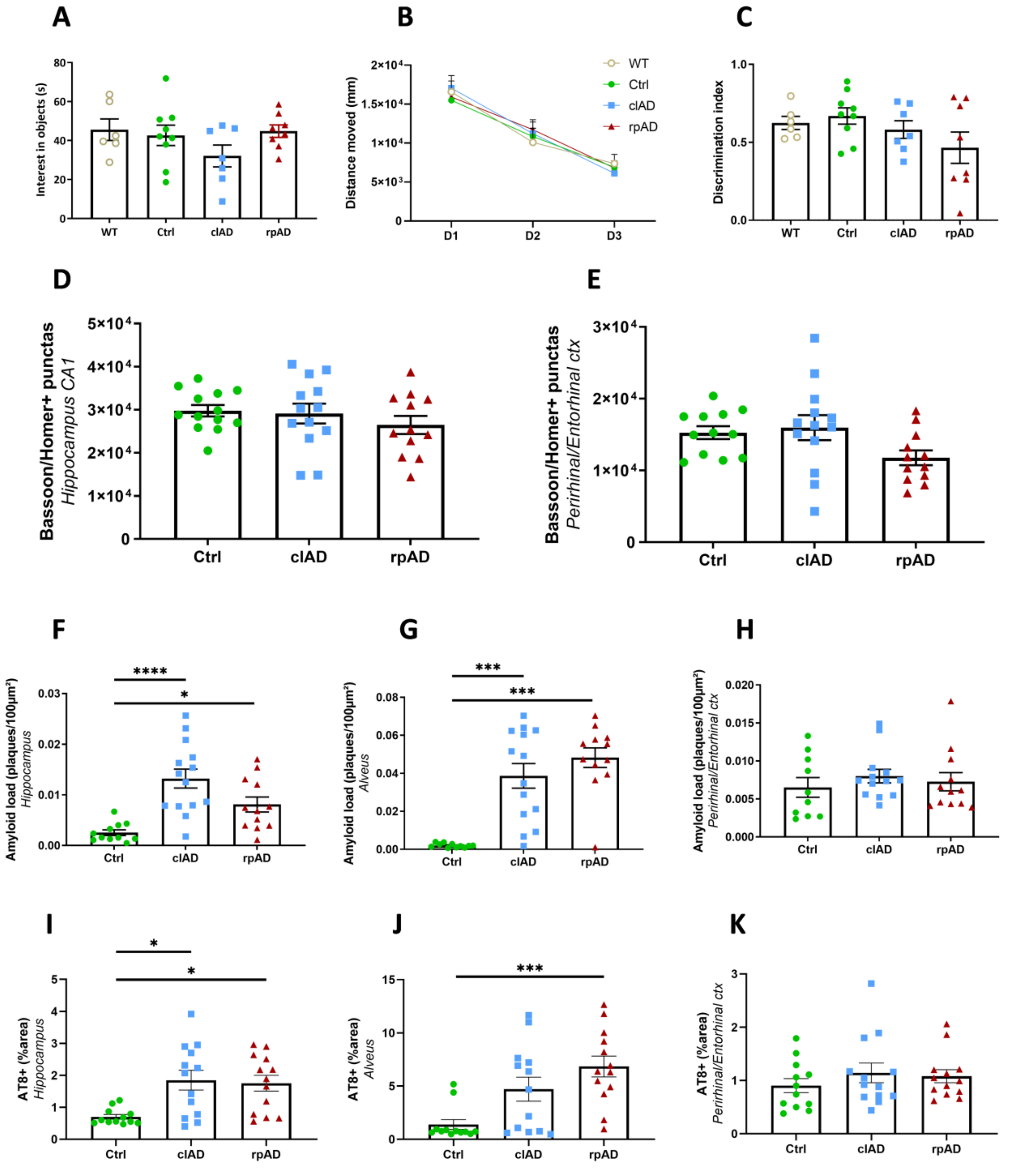

Supplementary Figure 4. Cognitive performance, synaptic density, amyloid and tau loads evaluations at 4 mpi. (A-C) Object recognition performances were evaluated at 4 mpi using a V-maze test. WT mice and APP$_{swe}$/PS1$_{dE9}$ mice inoculated with Ctrl, clAD or rpAD brain extracts had comparable exploratory activity, as suggested by the time spent on exploring the objects (A) ($p>0.05$; Kruskal-Wallis with Dunn's multiple comparisons) and the distance moved throughout the 3-day test (B) (for the days: $F_{(1.89, 49.15)} = 152.6$, $p<0.0001$; for the groups: $F_{(3, 26)} = 0.041$, $p=0.99$; two-way repeated measures ANOVA with the Geisser-Greenhouse correction and Dunnett's multiple comparisons). No difference in the novel object recognition test was reported between the groups, as similar discrimination indexes were observed (C) ($p>0.05$; Kruskal-Wallis with Dunn's multiple comparisons). (D-E) Quantification of Bassoon and Homer colocalization at 4 mpi did not show any differences in the CA1 (D) and in the perirhinal/entorhinal cortex (E) between the groups ($p>0.05$; Kruskal-Wallis with Dunn's multiple comparisons). (F-H) Amyloid load quantification at 4 mpi revealed that AD (clAD and rpAD) brain inoculation accelerates amyloid deposition in the alveus (F) and hippocampus (G), but not the perirhinal/entorhinal cortex (H) (respectively for clAD and rpAD mice, in the alveus $p=0.0008$ and 0.0003, in the hippocampus $p<0.0001$ and $p=0.041$, in the perirhinal/entorhinal cortex $p>0.05$; Kruskal-Wallis with Dunn's multiple comparisons). (I-K) AT8-positive tau overall quantification at 4 mpi revealed that AD (clAD and rpAD) brain inoculation induces tau lesions in the alveus (I) and hippocampus (J), but not the perirhinal/entorhinal cortex (K) (respectively for clAD and rpAD mice, in the alveus $p= 0.080$ and 0.0006, in the hippocampus $p= 0.016$ and 0.011, in the perirhinal/entorhinal cortex $p>0.05$; Kruskal-Wallis with Dunn's multiple comparisons). *$p<0.05$; ***$p<0.001$; ****$p<0.0001$. $n_{Ctrl}=11$, $n_{clAD}=14$, $n_{rpAD}=12$ mice. Data are shown as mean ± s.e.m.

Supplementary Figure 5

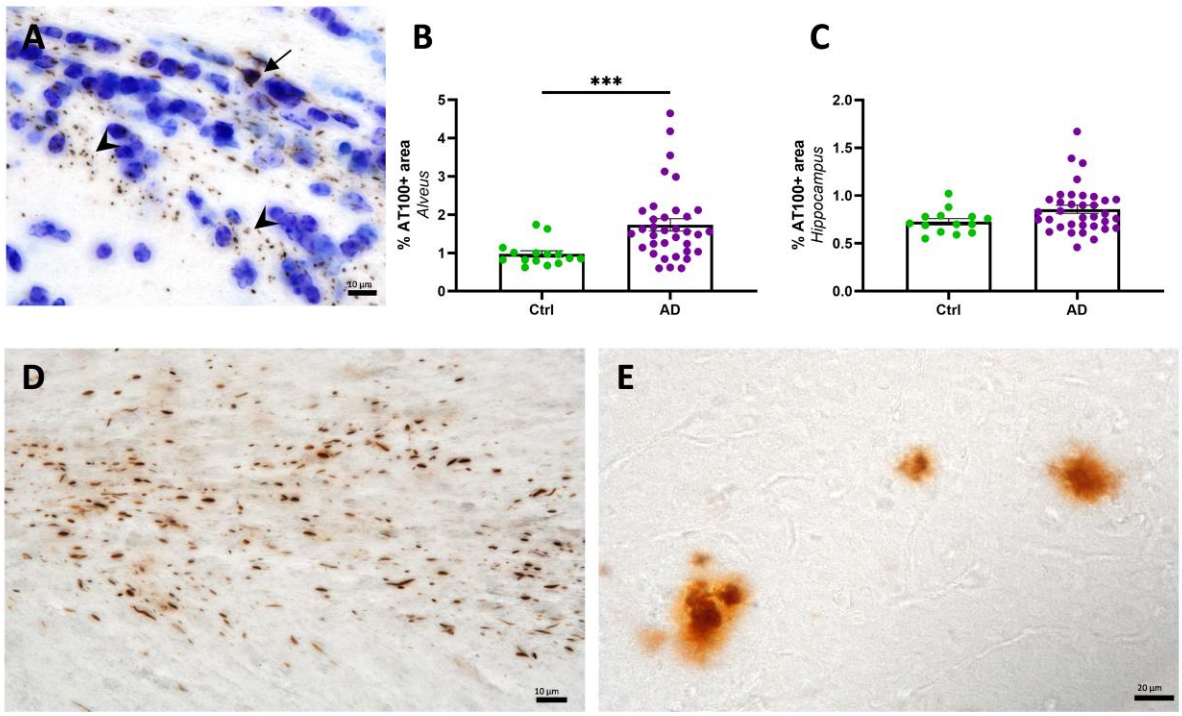

Supplementary Figure 5. AT100 and Gallyas-positive lesions next to the inoculation site of $\mathbf{APP_{swe}/PS1_{dE9}}$ mice 8 months after AD brain extracts injection. (A) AT100 staining revealed NTs (arrowheads) and NFTs (arrow). (B-C) Overall quantification of AT100 labeling showed increased labeling in the alveus (B) and a trend for increased labeling in the hippocampus (C) of AD inoculated mice (p=0.0007 and 0.092 respectively, Mann-Whitney test). Gallyas silver staining revealed neuropil threads (D) as well as amyloid plaques (E) in AD-inoculated mice. n_{Ctrl}=15, n_{AD}=35. Data are shown as mean ± s.e.m. Scale bars = 10 µm (A, D) and 20 µm (E).

Supplementary Figure 6

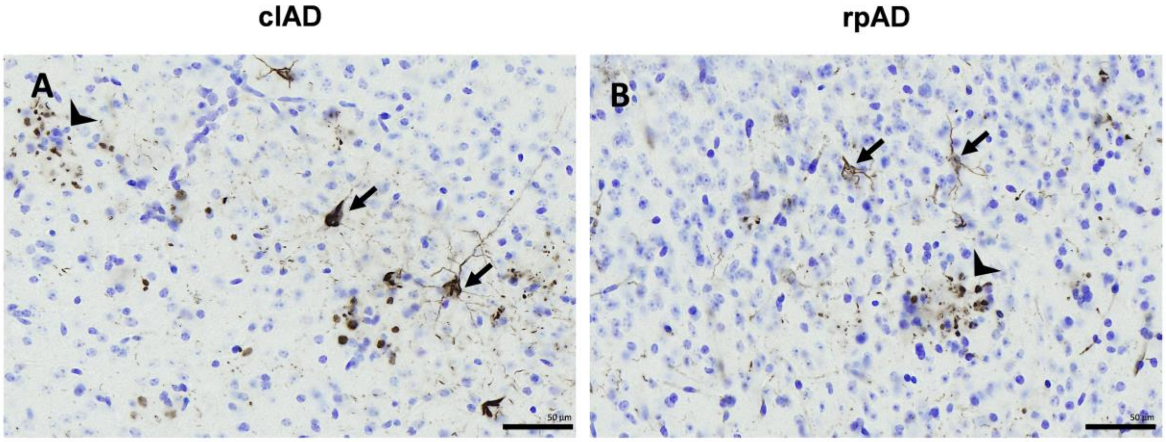

Supplementary Figure 6. AT8-positive lesions in the visual cortex of APP$_{swe}$/PS1$_{dE9}$ mice 8 months after AD brain extract inoculation. AT8 staining revealed NFTs (arrows) surrounded by neuropil threads, as well as neuritic plaques (arrowheads), in the visual cortex of clAD (A) and rpAD (B) brain-inoculated mice. Scale bars = 50 µm.

Supplementary Figure 7

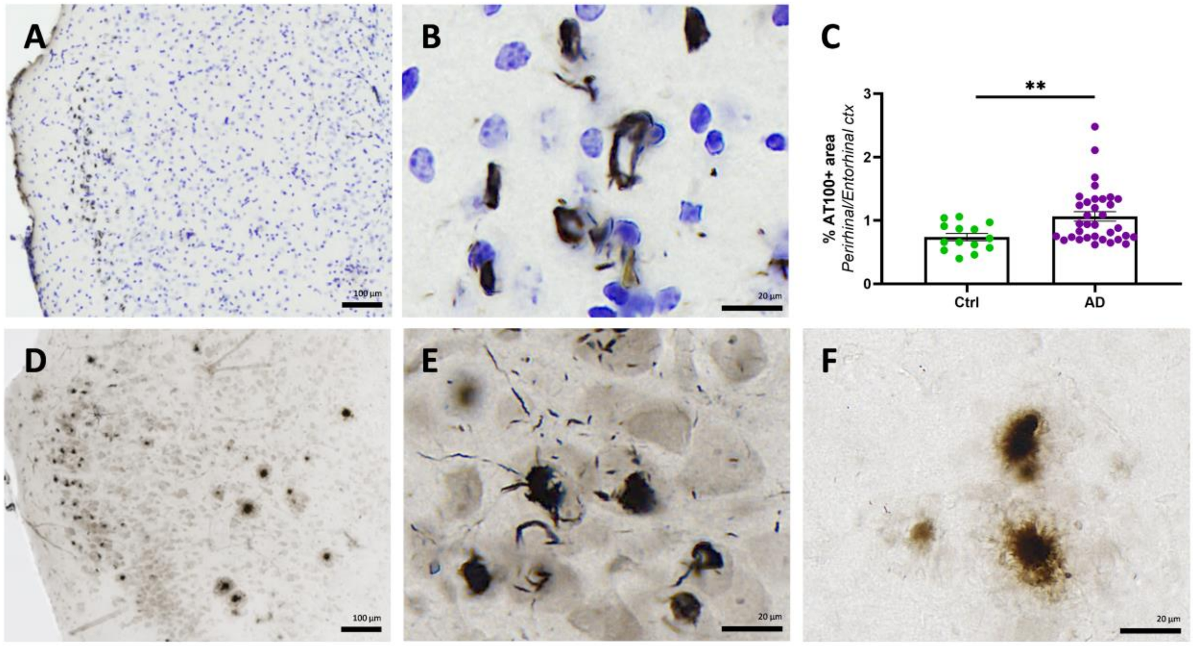

Supplementary Figure 7. AT100- and Gallyas-positive lesions spreading to the perirhinal/entorhinal cortex of APP$_{swe}$/PS1$_{dE9}$ mice 8 months after AD brain extract injection. (A-B) AT100 staining revealed NFTs in the perirhinal/entorhinal cortex. (C) Overall quantification of AT100 labelling showed increased labelling in the perirhinal/entorhinal cortex of AD-inoculated mice compared to Ctrl-inoculated ones (p=0.005, Mann-Whitney test). (D-F) Gallyas silver staining revealed labelled neurons evoking NFTs (E) as well as amyloid plaques (F). n$_{Ctrl}$=15, n$_{AD}$=35. Data are shown as mean ± s.e.m. Scale bars = 100 µm (A, D) and 20 µm (B, E, F).

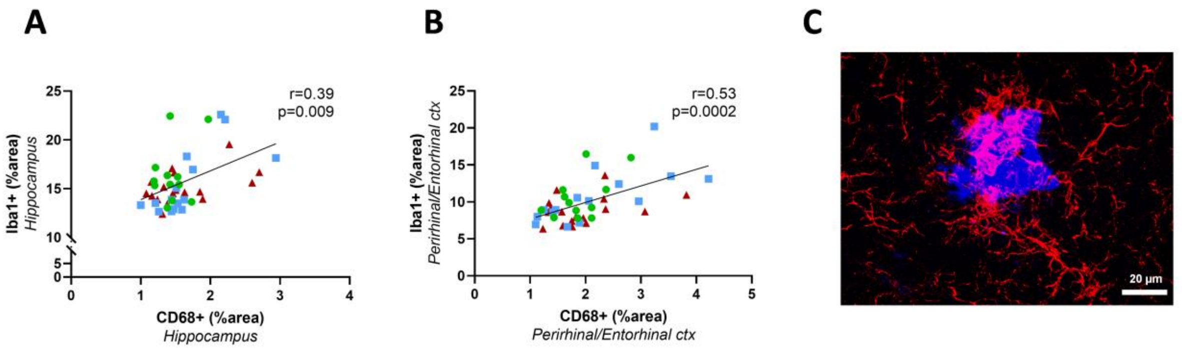

Supplementary Figure 8. Iba1 and CD68 staining. Iba1 staining level was correlated with CD68 labelling in the hippocampus (A) and in the perirhinal/entorhinal cortex (B). Confocal microscopy of Iba1-positive microglia surrounding amyloid deposition stained by MXO4 (C). Scale bar = 20µm.

Supplementary Figure 9

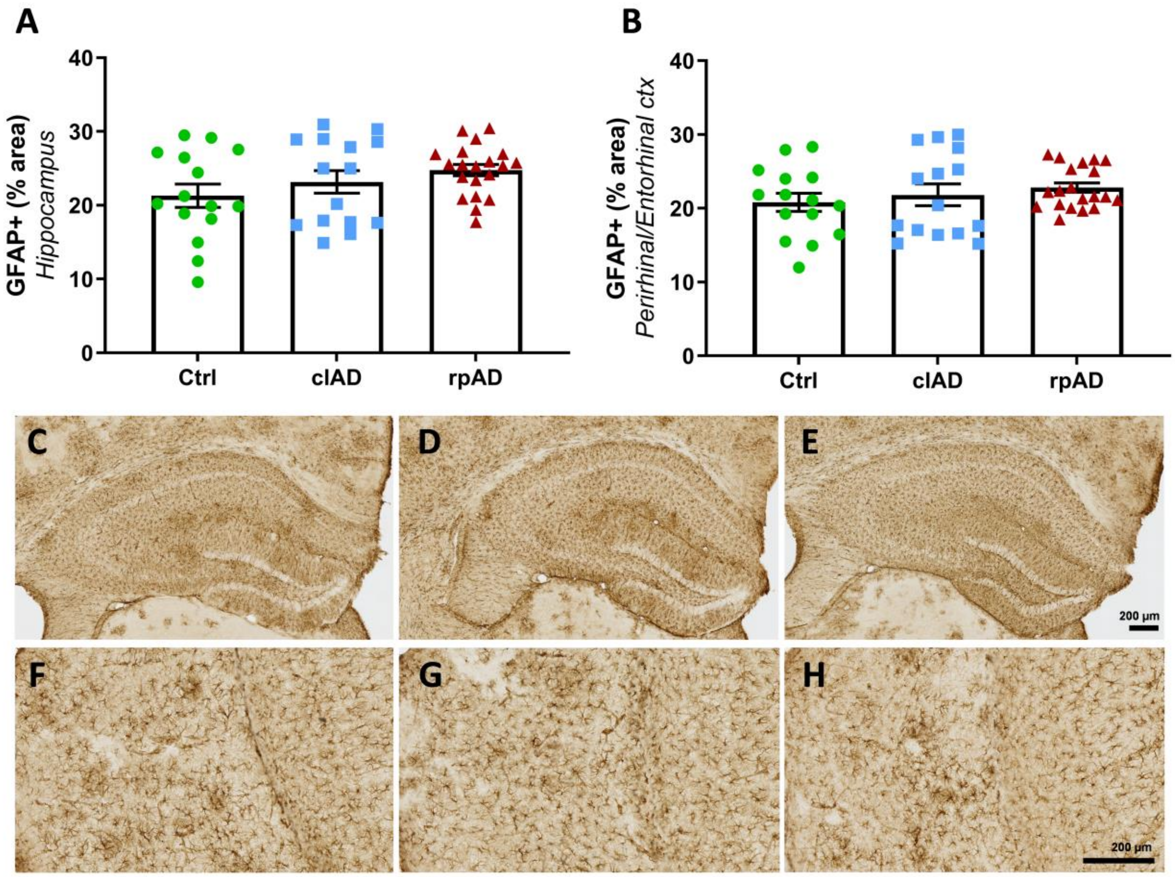

Supplementary Figure 9. Astrocytic coverage was similar in the hippocampus and perirhinal/entorhinal cortex of AD- and Ctrl-inoculated $APP_{swe}/PS1_{dE9}$ mice at 8 mpi. GFAP staining revealed similar astrocytic loads in the hippocampus (A, C-E) and perirhinal/enthorhinal cortex (B, F-H) of Ctrl, clAD and rpAD-inoculated $APP_{swe}/PS1_{dE9}$ mice at 8 mpi. n_{Ctrl}=15, n_{clAD}=15, n_{rpAD}=20 mice. Data are shown as mean ± s.e.m. Scale bars = 200 µm.